



Research paper



Stiffness optimization design of wheeled-legged rover integrating active and passive compliance capabilities

Bike Zhu, Jun He^{*}, Feng Gao

State Key Laboratory of Mechanical System and Vibration, School of Mechanical Engineering, Shanghai Jiao Tong University, Shanghai 200240, China

ARTICLE INFO

Keywords:

Wheeled-legged rover
Performance analysis
Kinematics
Active and passive compliance

ABSTRACT

Compliance capability is one of the most important properties of suspension systems for rough-terrain robots. This imposes specific requirements on system stiffness design, which directly determines the platform's performance in response to external stimuli. To address the challenge of stiffness optimization design in active and passive compliant systems, this paper proposes a novel and practical method for optimizing stiffness for a terrain-adaptive wheel-legged rover. Firstly, the kinematic model of this multi-degree-of-freedom platform is established. Secondly, the deformation capability coefficient, load capacity coefficient, energy efficiency coefficient, and dynamic stability coefficient are derived as performance indices to assess the behavior of the system. By establishing the relationship between joint configuration variation and system stiffness, stiffness parameters could be evaluated through these performance indices. Ultimately, the global optimum stiffness parameters are selected from the refined intersection of the individual performance optimal domains. Thirdly, the optimum parameters are calculated and applicability verified numerically. The designed parameters are verified experimentally on a wheeled-legged rover. The experimental results demonstrate that the proposed algorithm can find the parameter combination that achieves optimal system performance, thereby enhancing the system's terrain adaptability.

1. Introduction

With the advancement of extraterrestrial exploration, planetary rovers have become indispensable tools for human exploration of outer space. Wheeled-legged rovers, in particular, offer enhanced flexibility and terrain adaptability due to their increased degrees of freedom and active joints. The design of their suspension systems must incorporate compliance capabilities to ensure safety and stability, with elasticity being one of the most essential properties. It refers to the ability of the system to deform or undergo elastic deformation, allowing the rover to adapt to different terrains, absorb shocks, and enhance overall agility and stability. Currently, there are primarily two approaches to achieving suspension elasticity performance: one is through passive compliant mechanisms, and the other is through active compliance control methods.

Passive compliance refers to mechanical systems that possess general elastic-type kinematic characteristics. The use of elastic materials or mechanisms in the design of suspensions and joints can contribute to the efficiency and performance of robotic systems. Various compliant mechanisms have been developed employing elasticity [1], torsional springs [2], or similar mechanisms [3], all of

* Corresponding author.

E-mail address: jhe@sjtu.edu.cn (J. He).

which have demonstrated effective performance. Physical compliance utilization can be categorized into three groups based on setting locations and configurations: joint-parallel configured, joint-series configured, and leg-distal compliance [4]. Most legged robots fall into these categories. The StarIETH robot incorporates series compliance through SEA(Series Elastic Actuator)-based actuation [5,6]. Implementing joint series compliance endows the robot with complete torque control, enhances its energetic efficiency and ensures essential robustness for dynamic maneuvers. The Cheetaroid-II robot, designed by Na et al. [7], features joint parallel compliance structures. The Dynarobin robot [8] utilizes distal compliance structures with an articulated spin mechanism. Han et al. [9] utilize a passively adaptive spherical joint with a compressed spring installed at the ankle position for a legged lander. Lin et al. [10] achieved variable-curvature adaptability in a wall-climbing robot through a passive-compliant suspension mechanism, and investigated the kinematics transformation flow of the system. Certain legged robots employ multiple forms of compliance. For example, Cheetah-Cub achieves leg-distal compliance and series-configured compliance by employing a biarticulated spring in the leg segment and a helical spring in the distal joint [11]. Roozing et al. [12] introduce the eLeg, a system that incorporates both series- and parallel-elastic actuation, along with a biologically inspired biarticular tendon. Active compliance involves integrating actuators or control devices into the mechanical system, enabling the system to actively modify its response or behavior in real time based on external stimuli or commands. It can be achieved through compliant control algorithms [13]. Impedance control is commonly implemented on robotic systems. Xu et al. [14] propose a novel event-based disturbance control and whole-body stability control method for a contact-redundant hexapod robot, enabling it to stably navigate rough terrain by accurately detecting disturbed legs and optimizing ground reaction forces to maintain trunk stability.

Many achievements have been made in the field of active and passive compliant mechanism design. Okada et al. [15] introduce a design principle for active and passive hybrid compliance that takes into account the frequency domain. This method utilized mechanical elasticity to realize passive compliance and control theories to realize active compliance. Gurney et al. [16] present the Uped robot with compliant legs. This paper focuses on the design of the system which is capable of adjusting compliance parameters and studying the effects of compliance parameters on the performance of the robot.

Nomenclature

| | | |
|----------------|-----------------|--|
| l_b | $i = 1 \dots 5$ | Length of the link i |
| l_Δ | | Length of the link between point P and point D |
| $l_{\Delta 5}$ | | Length of link 5 without the spring |
| l_{sp} | | Length of the spring |
| l_{sp0} | | Initial length of the spring |
| θ_b | $i = 1 \dots 5$ | Position of driven joints |
| ψ_b | $i = 1, 2$ | Rotational joint angle |
| ψ_Δ | | A constant joint offset between link l_Δ and link l_5 |
| q_L | | Driven joint vector of each leg |
| q_B | | Driven joint vector of the whole body |
| q_S | | Driven joint vector of the five-bar mechanism |
| q_H | | Driven joint vector of the steering joint and side swing joint |
| τ | | Torque vector of driven joint |
| J | | Jacobian matrix |
| \bar{J} | | Force jacobian matrix |
| H | | Hessian matrix |
| R | | Rotation matrix |
| v | | Linear velocity |
| ω | | Angular velocity |
| a | | Linear acceleration |
| ϵ | | Angular acceleration |
| f | | Position of the end-effector |
| ${}^B h$ | | Position vector from frame $\{H\}$ to frame $\{B\}$ |
| s_1 | | Unit direction vector along the z -axis |
| s_2 | | Unit direction vector along the x -axis |
| F_{IN} | | Ground reaction force |
| F_r | | Reaction force along the direction of spring compression |
| F_d | | Desired contact force |
| M_A | | Inertial matrix of impedance control |
| B_A | | Damping matrix of impedance control |
| K_A | | Stiffness matrix of impedance control |
| k | | Stiffness of the spring |
| k_{eq} | | Equivalent stiffness |
| σ | | Angle between the input force and the direction vector of the calf |
| φ | | Slop angle |
| k_J | | Stiffness of the motor driver |
| K_P | | Stiffness matrix of the system |
| K_f | | Translational stiffness of the system |
| K_t | | Rotational stiffness of the system |
| K_c | | Coupling stiffness of the system |
| S | | Deformation matrix |
| λ | | Eigenvector |
| η_S | | Deformation coefficient |

(continued on next page)

(continued)

| | |
|--|--|
| η_C | Load capacity coefficient |
| η_{ACE} | Active Compliance Energy (ACE) distribution coefficient |
| η_N | System stability coefficient |
| η_{ave} | Comprehensive performance coefficient |
| $T_{sm}, m = 1 \dots 4$ | Combined torque exerted on the supporting edge |
| $T_{pm}, m = 1 \dots 4$ | Combined torque exerted on the supporting point |
| $p_m, m = 1 \dots 4$ | Position vector of the supporting points |
| P_E | Position vector of the load's CoM |
| P_B | Position vector of the body's CoM |
| $r_m, m = 1 \dots 4$ | Position vector from the wheel center to the contact point |
| r_{ij} | Position vector of the CoM of link l_{ij} |
| $l_m, m = 1 \dots 4$ | Vector of the supporting edge |
| F_B, T_B | Force and torque acting on the rover's body |
| F_E, T_E | External force and torque acting on the body |
| $F_{lj}, T_{lj}, i = 1 \dots 4, j = 1 \dots 6$ | Force and torque acting on the link l_{ij} |
| μ | Load factor of the spring |
| $F_{G\max}$ | Maximum load that the rover can carry (including its own weight) |
| Ω | Index domain |

Nasr et al. [17] developed an optimal design method for passive and active assistive shoulder exoskeletons. The system design is optimized by choosing features of the passive mechanism and active exoskeleton motors. They propose multiple criteria such as the human joint variables and signals as well as practical manufacturing criteria for optimization. In addition, geometric errors directly affect the position accuracy of robot end-effectors. Brahmia et al. [18] consider the kinematic sensitivity and achieve the identification of the most crucial geometric errors for parallel and serial robotic systems. Other studies have explored designs such as active/passive variable stiffness actuators [19], optional passive/active wheeled-legged robots [20], etc. The stiffness design of active and passive compliant systems has been an active research area, with researchers approaching the problem from various perspectives and based on different criteria.

Designing a compliant robotic system poses greater challenges compared to rigid bodies, especially when there are multiple optimization objectives. There are some widely used multi-objective optimization algorithms such as the ant colony algorithm [21], particle swarm algorithm [22], genetic algorithm [23], and other heuristic intelligence algorithms. Brahmia et al. [24] propose a novel optimization method based on the interior-point algorithm to allocate tolerances for the geometric parameters of a Delta parallel robot. Another commonly used multi-objective optimization method in mechanism design is the performance atlas method [25–28]. The performance atlas method provides a transparent understanding of the trade-offs between conflicting objectives, and facilitates informed decision-making in multi-objective optimization problems. It relies on the designer's subjective judgment and choices, allowing the designer to determine the optimal solution through perceptual visualization. Russo et al. [29] utilize this method to optimize four different objective functions and get optimal geometrical proportions for the design of a parallel robotic leg. Liu et al. [30] designed a planar 5R symmetrical parallel mechanism by defining and analyzing its performance indices. These indices are graphically presented in design space to achieve the optimal dimensional mechanism. Han et al. [31] utilize the performance atlas method to evaluate the operational capability of a reconfigurable legged mobile lander (ReLML). In summary, the performance atlas method can achieve graphical representations of performances and has been widely applied in the design process of mechanical systems.

This paper adopts the performance atlas method to address the stiffness optimization design problem of active-passive compliance systems. Specifically, the prototype utilized in this paper is a terrain-adaptive wheel-legged (TAWL) rover with active and passive compliance capabilities. Based on our previous work on its motion planning [32], kinematic design and position control [33], this paper focuses on its stiffness optimization design. The optimization purpose is to maintain overall optimum performance for the rover while traversing slopes. The challenges addressed by this work include comprehensively evaluating the performance of active-passive compliant systems and solving the multi-objective optimization problem. In previous studies, indices such as the cost of transport and joint variables have been insufficient for fully analyzing the capabilities of active-passive compliant wheeled-legged rovers. This paper introduces new indices that evaluate these rovers in terms of energy consumption, load capacity, motion stability, and terrain adaptability. Additionally, to solve the multi-objective optimization problem, the performance atlas method is employed to facilitate informed decision-making. This paper enhances the traditional performance atlas method by eliminating the need for spatial models and dimensionless optimization variables. Instead, it adopts the visualization optimization technique derived from the performance atlas method to optimize variables with varying dimensions. Main contributions of this paper are:

- (1) The kinematic and dynamic models of a wheeled-legged robotic system with 20 active joints and passive springs are established. The deformation capability coefficient, load capacity coefficient, energy efficiency coefficient, and dynamic stability coefficient are derived to assess the behavior of the system.
- (2) A novel and practical stiffness optimization design method for active/passive compliant robotic systems is proposed. The performance atlas method is utilized to determine the global optimum region and to find the optimal stiffness parameters.
- (3) The proposed method and designed parameters are analyzed and verified both numerically and experimentally on the wheeled-legged TAWL rover.

The remainder of this paper is organized as follows: [Section 2](#) introduces the structure and the kinematic model of the system. [Section 3](#) derives the performance indices in terms of passive and active compliance capabilities. [Section 4](#) describes the optimization parameters and constraint conditions. [Section 5](#) implements the optimization design, calculates the optimum parameters, and verifies the results through experiments. [Section 6](#) concludes the paper.

2. System overview and kinematic analysis

2.1. System overview

The TAWL rover has four identical legs, with each leg having 5 driving joints, and the whole system has 20 DoFs (Degrees of Freedom), as shown in [Fig. 1](#). The rover's body is equipped with an onboard power supply, a motion algorithm processor, a visual algorithm processor, and an IMU (Inertial Measurement Unit). The system employs force sensors to measure the ground reaction force, and then actively adjust its configuration to regulate the leg length and the position of the foot. Each leg's upper part consists of a five-bar mechanism with a zero-length base link, while the lower part is connected to a passive spring. In [Fig. 2](#), (a) refers to the active compliance mechanisms. The design of these mechanisms is aimed at improving rover stability and enhancing load capacity. [Fig. 2\(b\)](#) refers to the passive spring-damper mechanisms. A telescopic mechanism incorporating a passive damped spring is employed. The compliant leg is equipped with two spring-loaded ball plungers capable of activating the spring-damper system. When the ground reaction force exceeds the threshold of the spring-loaded ball plunger, the spring-damper mechanism is triggered and can effectively absorb impact energy. The main focus of passive springs is to effectively manage uncertainties and disturbances during uneven terrains. Therefore, the rover is capable of actively and passively complying to the ground during navigation.

2.2. Kinematics model

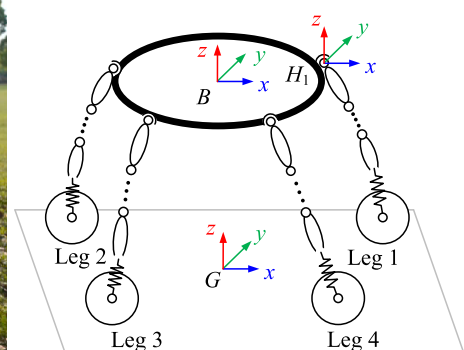
This section introduces the velocity and acceleration model of the system. The body coordinate system, denoted as $\{B\}$, is defined with its origin at the center of the body. The z -axis of $\{B\}$ is perpendicular to the surface of the body, and the x -axis is aligned with the direction of the forward movement. The ground coordinate system, denoted as $\{G\}$, has its origin at the projection of $\{B\}$ onto the ground when the rover is initially positioned. The z -axis of $\{G\}$ is perpendicular to the ground, and the x -axis of $\{G\}$ is parallel to the x -axis of $\{B\}$. For each leg of the rover, from the body to the end-effector (located at the wheel center), there are two rotational joints, with the rotational axes intersecting the origin of the hip coordinate system $\{H\}$. The origin of $\{H\}$ is fixed to the body and does not rotate with the driven joints. Then there is the planar five-bar mechanism, along with the spring system and the wheel. A constant offset angle ψ_Δ exists between l_Δ and l_5 . This part of the leg is defined in the $\{S\}$ coordinate system. The x -axis direction of the frame $\{S\}$ is parallel to the x -axis direction of $\{H\}$, but their z -axis directions are opposite. Each leg has 6 links, with the link 6 defined as the wheel. Point F is defined as the end-effector of the leg. A spring is installed between link 5 and link 6, with an elasticity constant of k , a length of l_{sp} , and an initial length of l_{sp0} . It can only be deformed along the axial direction of link 5, as shown in [Fig. 3](#). Define the input vector of each leg as $\mathbf{q}_L = [\theta_1, \theta_2, \theta_3, \theta_4, \theta_5, 0]^T$, the input vector of the whole system as $\mathbf{q}_B = [\mathbf{q}_{L1}^T, \mathbf{q}_{L2}^T, \mathbf{q}_{L3}^T, \mathbf{q}_{L4}^T]^T$.

In the coordinate system of $\{S\}$, the position of point P is denoted as (x_p, z_p) . According to geometric constraints, it can be derived as

$$\begin{cases} (x_p - l_3 c_4)^2 + (z_p - l_3 s_4)^2 = l_4 \\ (x_p - l_2 c_3)^2 + (z_p - l_2 s_3)^2 = l_\Delta \end{cases} \quad (1)$$



(a) Prototype of the TAWL rover



(b) Geometry and topology of the TAWL rover

Fig. 1. Prototype and topology of the TAWL rover.

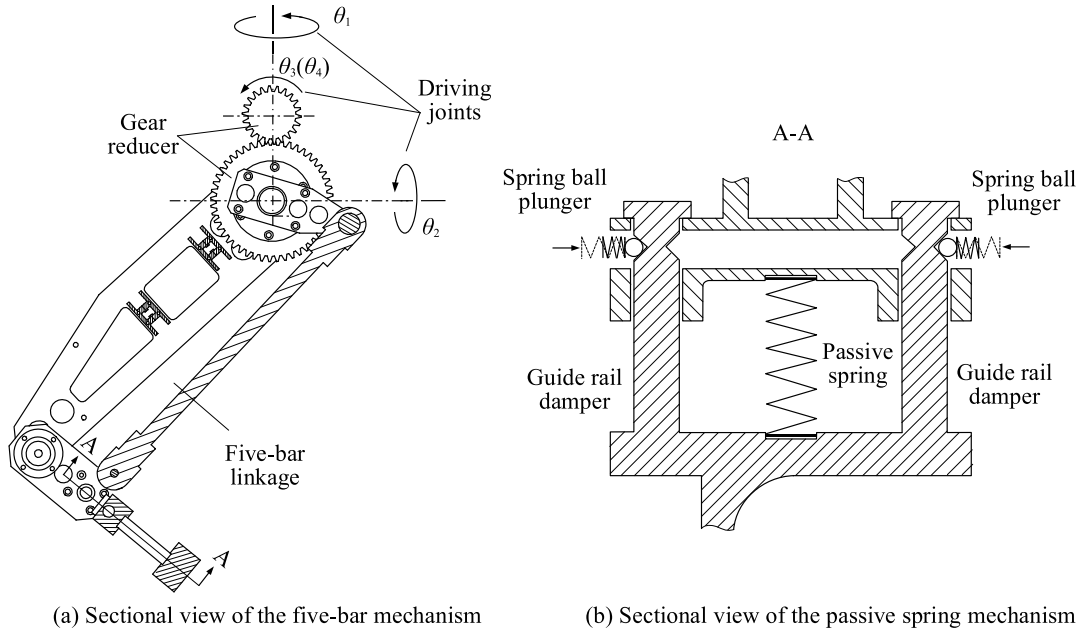


Fig. 2. Sectional view of active and passive compliance mechanisms.

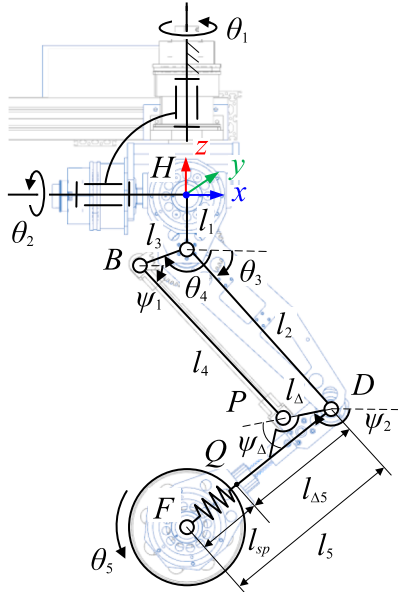


Fig. 3. Diagram of legmechanism integrating active and passive compliance.

Differentiating Eq. (1) with respect to time yields the velocity equation of point P . It can be written in the matrix form as

$${}^S\mathbf{J}_{XP} {}^S\dot{\mathbf{X}}_P = {}^S\mathbf{J}_q \dot{\mathbf{q}}_S \Rightarrow {}^S\dot{\mathbf{X}}_P = {}^S\mathbf{J}_P \dot{\mathbf{q}}_S \quad (2)$$

The angular velocity of link l_5 is equivalent to the combined velocities $\dot{\theta}_3$ and $\dot{\psi}_2$,

$$\omega_{Py} = \dot{\theta}_3 + \dot{\psi}_2 \quad (3)$$

Differentiating Eq. (2) with respect to time yields the acceleration equation of point P in the coordinate system of $\{S\}$, which can be written in the matrix form as

$$\begin{aligned} {}^S J_{XP} {}^S \ddot{\mathbf{X}}_P &= {}^S J_q \ddot{\mathbf{q}}_S + \dot{\mathbf{q}}_S^T {}^S \mathbf{H}_q \dot{\mathbf{q}}_S = {}^S J_q \ddot{\mathbf{q}}_S + \dot{\mathbf{q}}_S^T \tilde{\mathbf{H}}_q \dot{\mathbf{q}}_S \\ \Rightarrow {}^S \ddot{\mathbf{X}}_P &= {}^S J_P \ddot{\mathbf{q}}_S + \dot{\mathbf{q}}_S^T {}^S \mathbf{H}_P \dot{\mathbf{q}}_S \end{aligned} \quad (4)$$

where ${}^S \mathbf{H}_q$ is a $4 \times 4 \times 2$ dimensional matrix, $\tilde{\mathbf{H}}_q$ and ${}^S \mathbf{H}_P$ are $2 \times 2 \times 2$ dimensional matrices.

The relationship between ψ_2 and \mathbf{q}_S can be obtained from position kinematics. Therefore, ${}^S \dot{\mathbf{X}}_P$ and ${}^S J_P$ can be extended to 6×1 and 6×2 dimensions. The velocity relationship between point F and point P in the coordinate system of $\{S\}$ satisfies

$${}^S \dot{\mathbf{X}}_P = \begin{bmatrix} {}^S \mathbf{v}_F \\ {}^S \boldsymbol{\omega}_F \end{bmatrix} = \begin{bmatrix} \mathbf{I} & -{}^S \mathbf{r}_{PF} \times \\ \mathbf{0} & \mathbf{I} \end{bmatrix} {}^S \dot{\mathbf{X}}_P = \begin{bmatrix} \mathbf{I} & -{}^S \mathbf{r}_{PF} \times \\ \mathbf{0} & \mathbf{I} \end{bmatrix} {}^S J_P \dot{\mathbf{q}}_S = {}^S J_L \dot{\mathbf{q}}_S \quad (5)$$

where \mathbf{r}_{PF} is the position vector from point P to point F .

Differentiating Eq. (4) with respect to time yields the acceleration equation of point F in the coordinate system of $\{S\}$, which can be written in the matrix form as

$${}^S \ddot{\mathbf{X}}_F = \begin{bmatrix} \mathbf{I} & -{}^S \mathbf{r}_{PF} \times \\ \mathbf{0} & \mathbf{I} \end{bmatrix} {}^S \ddot{\mathbf{X}}_P + \begin{bmatrix} \mathbf{0} & -{}^S \dot{\mathbf{r}}_{PF} \times \\ \mathbf{0} & \mathbf{0} \end{bmatrix} {}^S \dot{\mathbf{X}}_P = {}^S J_L \ddot{\mathbf{q}}_S + \dot{\mathbf{q}}_S^T {}^S \mathbf{H}_L \dot{\mathbf{q}}_S + {}^S \tilde{\boldsymbol{\omega}}_F \times {}^S J_L \dot{\mathbf{q}}_S \quad (6)$$

The first two rotation joints are denoted as θ_1 and θ_2 , separately. Assuming the unit direction vector along the z -axis is \mathbf{s}_1 , and along the x -axis is \mathbf{s}_2 . In the coordinate system of $\{H\}$, the velocity of point F is written as

$$\begin{cases} {}^H \mathbf{v}_F = \dot{\theta}_1 \mathbf{s}_1 \times {}^H \mathbf{f} + \dot{\theta}_2 \mathbf{s}_2 \times {}^H \mathbf{f} + {}^H \mathbf{R} {}^S \mathbf{R} {}^S \mathbf{v}_F \\ {}^H \boldsymbol{\omega}_F = \dot{\theta}_1 \mathbf{s}_1 + \dot{\theta}_2 \mathbf{s}_2 + {}^H \mathbf{R} {}^S \boldsymbol{\omega}_F \end{cases} \quad (7)$$

where ${}^H \mathbf{f}$ is the position vector of point F in the frame $\{H\}$,

$${}^H \mathbf{R} = \text{rot}(\mathbf{s}_1, \theta_1) \text{rot}(\mathbf{s}_2, \theta_2 + \pi) = \begin{bmatrix} \mathbf{c}_1 & \mathbf{s}_1 \mathbf{c}_2 & -\mathbf{s}_1 \mathbf{s}_2 \\ \mathbf{s}_1 & -\mathbf{c}_1 \mathbf{c}_2 & \mathbf{c}_1 \mathbf{s}_2 \\ \mathbf{0} & -\mathbf{s}_2 & -\mathbf{c}_2 \end{bmatrix}$$

Writing Eq. (7) into the matrix form, the Jacobian matrix of the end-effector in the hip coordinate is expressed as

$${}^H \dot{\mathbf{X}}_F = \begin{bmatrix} {}^H \mathbf{R} & \mathbf{0} \\ \mathbf{0} & {}^H \mathbf{R} \end{bmatrix} {}^S J_L \begin{bmatrix} \dot{\theta}_3 \\ \dot{\theta}_4 \end{bmatrix} + \begin{bmatrix} \mathbf{s}_1 \times {}^H \mathbf{f} & \mathbf{s}_2 \times {}^H \mathbf{f} \\ \mathbf{s}_1 & \mathbf{s}_2 \end{bmatrix} \begin{bmatrix} \dot{\theta}_1 \\ \dot{\theta}_2 \end{bmatrix} = {}^H J_L \dot{\mathbf{q}}_L \quad (8)$$

Differentiating Eq. (7) with respect to time yields the acceleration equation of point F in the coordinate system of $\{H\}$,

$$\begin{cases} {}^H \ddot{\mathbf{a}}_F = {}^H \mathbf{R} {}^S \ddot{\mathbf{a}}_F + {}^S \boldsymbol{\omega}_F \times {}^H \mathbf{R} {}^S \mathbf{v}_F + \ddot{\theta}_1 \mathbf{s}_1 \times {}^H \mathbf{f} + \ddot{\theta}_2 \mathbf{s}_2 \times {}^H \mathbf{f} + \dot{\theta}_1 (\mathbf{R}_{\theta_2} {}^S \boldsymbol{\omega}_F \times \mathbf{s}_1) \times {}^H \mathbf{f} + \dot{\theta}_2 ({}^S \boldsymbol{\omega}_F \times \mathbf{s}_2) \times {}^H \mathbf{f} + \dot{\theta}_1 \mathbf{s}_1 \times {}^H \dot{\mathbf{f}} + \dot{\theta}_2 \mathbf{s}_2 \times {}^H \dot{\mathbf{f}} \\ {}^H \ddot{\mathbf{e}}_F = {}^H \mathbf{R} {}^S \ddot{\mathbf{e}}_F + {}^S \boldsymbol{\omega}_F \times {}^H \mathbf{R} {}^S \boldsymbol{\omega}_F + \ddot{\theta}_1 \mathbf{s}_1 + \ddot{\theta}_2 \mathbf{s}_2 + \dot{\theta}_1 (\mathbf{R}_{\theta_2} {}^S \boldsymbol{\omega}_F \times \mathbf{s}_1) + \dot{\theta}_2 ({}^S \boldsymbol{\omega}_F \times \mathbf{s}_2) \end{cases} \quad (9)$$

It can be written in the matrix form as

$$\begin{aligned} {}^H \ddot{\mathbf{X}}_F &= {}^H \tilde{\mathbf{R}} {}^S \ddot{\mathbf{X}}_L + {}^S \tilde{\boldsymbol{\omega}}_F \times {}^H \tilde{\mathbf{R}} {}^S \dot{\mathbf{X}}_L + {}^{H1} \mathbf{J}_L \ddot{\mathbf{q}}_H + {}^S \boldsymbol{\omega}_F {}^{H2} \mathbf{J}_L \dot{\mathbf{q}}_L + \dot{\mathbf{q}}_L^T {}^{H2} \mathbf{H}_L \dot{\mathbf{q}}_L \\ \Rightarrow {}^H \ddot{\mathbf{X}}_F &= {}^H \mathbf{J}_L \ddot{\mathbf{q}}_L + \dot{\mathbf{q}}_L^T {}^{H2} \mathbf{H}_L \dot{\mathbf{q}}_L + {}^{HH} \mathbf{J}_L \dot{\mathbf{q}}_L \end{aligned} \quad (10)$$

where \mathbf{R}_{θ_2} represents the rotation matrix introduced by the driven joint θ_2 ,

$${}^H \mathbf{H}_{L(:,1)} = \begin{bmatrix} \mathbf{s}_1 \times {}^H \mathbf{J}_{L(1:3)} & \mathbf{0} \\ \mathbf{0} & \mathbf{s}_2 \times {}^H \mathbf{J}_{L(1:3)} \\ \mathbf{0} & \mathbf{0} \end{bmatrix}, {}^H \mathbf{H}_{L(:,2)} = \mathbf{0}$$

$${}^{H1} \mathbf{J}_L = \begin{bmatrix} \mathbf{s}_1 \times {}^H \mathbf{f} & \mathbf{s}_2 \times {}^H \mathbf{f} \\ \mathbf{s}_1 & \mathbf{s}_2 \end{bmatrix}, {}^{H2} \mathbf{J}_L = \begin{bmatrix} \mathbf{R}_{\theta_2} \times \mathbf{s}_1 \times {}^H \mathbf{f} & \times \mathbf{s}_2 \times {}^H \mathbf{f} \\ \mathbf{R}_{\theta_2} \times \mathbf{s}_1 & \times \mathbf{s}_2 \end{bmatrix}, {}^H \mathbf{J}_L = \begin{bmatrix} {}^{H1} \mathbf{J}_L & \mathbf{0} \\ \mathbf{0} & {}^H \tilde{\mathbf{R}} {}^S \mathbf{J}_L \end{bmatrix}$$

$${}^H \tilde{\mathbf{R}} = \begin{bmatrix} {}^H \mathbf{R} & \mathbf{0} \\ \mathbf{0} & {}^H \mathbf{R} \end{bmatrix}, {}^S \tilde{\boldsymbol{\omega}}_F = \begin{bmatrix} {}^S \boldsymbol{\omega}_F & \mathbf{0} \\ \mathbf{0} & {}^S \boldsymbol{\omega}_F \end{bmatrix}, \mathbf{q}_H = [\theta_1 \quad \theta_2]^T$$

The velocity of the body in the ground frame $\{G\}$ is denoted as ${}^G \dot{\mathbf{X}}_B = [{}^G \mathbf{v}_B^T \quad {}^G \boldsymbol{\omega}_B^T]^T$. The velocity equation of each end-effector in the corresponding hip frame $\{H_j\}$ is denoted as ${}^{Hj} \dot{\mathbf{X}}_{F_j} = [{}^{Hj} \mathbf{v}_{F_j}^T \quad {}^{Hj} \boldsymbol{\omega}_{F_j}^T]^T$. Therefore, the velocity equation of each end-effector in the ground frame $\{G\}$ can be expressed as

$$\begin{cases} {}^G \boldsymbol{\nu}_{F_j} = {}^G \boldsymbol{\nu}_B + {}^G \boldsymbol{\omega}_B \times {}^G \mathbf{R} \left({}^B_{H_j} \mathbf{R}^{H_j} \boldsymbol{f}_j + {}^B \boldsymbol{h}_j \right) + {}^G \mathbf{R}_{H_j}^B \mathbf{R}^{H_j} \boldsymbol{\nu}_{F_j} \\ {}^G \boldsymbol{\omega}_{F_j} = {}^G \boldsymbol{\omega}_B + {}^G \mathbf{R}_{H_j}^B \mathbf{R}^{H_j} \boldsymbol{\omega}_{F_j} \end{cases} \quad (11)$$

where ${}^B \boldsymbol{h}_j$ is the position vector from frame $\{H_j\}$ to frame $\{B\}$.

Writing Eq. (11) in the matrix form leads to

$$\begin{aligned} {}^G \dot{\mathbf{X}}_{F_j} &= \left[\begin{array}{cc} \mathbf{I} & -{}^G \mathbf{R} \left({}^B_{H_j} \mathbf{R}^{H_j} \boldsymbol{f}_j + {}^B \boldsymbol{h}_j \right) \times \\ \mathbf{0} & \mathbf{I} \end{array} \right] {}^G \dot{\mathbf{X}}_B + \left[\begin{array}{cc} {}^G \mathbf{R}_{H_j}^B \mathbf{R} & \mathbf{0} \\ \mathbf{0} & {}^G \mathbf{R}_{H_j}^B \mathbf{R} \end{array} \right] {}^H \dot{\mathbf{X}}_{F_j} \\ \Rightarrow {}^G \dot{\mathbf{X}}_B &= {}^G_{F_j} \mathbf{J}^G \dot{\mathbf{X}}_{F_j} + {}^G_{F_j} \mathbf{J}_{H_j}^G \tilde{\mathbf{R}}^{H_j} \mathbf{J}_{L_j} \dot{\mathbf{q}}_{L_j} = {}^G_{F_j} \mathbf{J}^G \dot{\mathbf{X}}_{F_j} + {}^G_{L_j} \mathbf{J}_{L_j} \dot{\mathbf{q}}_{L_j} \end{aligned} \quad (12)$$

where

$$\begin{aligned} {}^G_{F_j} \mathbf{J} &= \left[\begin{array}{cc} \mathbf{I} & \left({}^G \mathbf{R}_{H_j}^B \mathbf{R}^{H_j} \boldsymbol{f}_j + {}^G \mathbf{R}^B \boldsymbol{h}_j \right) \times \\ \mathbf{0} & \mathbf{I} \end{array} \right], {}^G_{H_j} \tilde{\mathbf{R}} = \left[\begin{array}{cc} {}^G \mathbf{R}_{H_j}^B \mathbf{R} & \mathbf{0} \\ \mathbf{0} & {}^G \mathbf{R}_{H_j}^B \mathbf{R} \end{array} \right] \\ {}^G \mathbf{J}_{L_j} &= {}^G_{F_j} \mathbf{J}_{H_j}^G \tilde{\mathbf{R}}^{H_j} \mathbf{J}_{L_j} \end{aligned}$$

For the whole system, the Jacobian matrix is written as

$${}^B \mathbf{J}_I {}^G \dot{\mathbf{X}}_B = {}^G \mathbf{J}^G \dot{\mathbf{X}}_F + {}^G \mathbf{J}_B \dot{\mathbf{q}}_B \quad (13)$$

where ${}^B \mathbf{J}_I$ is a 24×6 dimensional matrix, ${}^B \mathbf{J}_I = [{}^I_{6 \times 6} \quad {}^I_{6 \times 6} \quad {}^I_{6 \times 6} \quad {}^I_{6 \times 6}]^T$.

If the wheel is in complete contact with the ground with no slippage, then ${}^G \ddot{\mathbf{X}}_{F_j} = 0$. Mark the acceleration of the body in the frame $\{G\}$ as ${}^G \ddot{\mathbf{X}}_B = [{}^G \mathbf{a}_B^T \quad {}^G \boldsymbol{\epsilon}_B^T]^T$. The acceleration of each end-effector in the corresponding hip frame $\{H_j\}$ is marked as ${}^H \ddot{\mathbf{X}}_{F_j} = [{}^H_j \mathbf{a}_{F_j}^T \quad {}^H_j \boldsymbol{\epsilon}_{F_j}^T]^T$. The acceleration of each end-effector in the frame $\{G\}$ is marked as ${}^G \ddot{\mathbf{X}}_{F_j} = [{}^G \mathbf{a}_{F_j}^T \quad {}^G \boldsymbol{\epsilon}_{F_j}^T]^T$, which can be obtained by differentiating Eq. (11) with respect to time,

$$\begin{cases} {}^G \mathbf{a}_{F_j} = {}^G \mathbf{a}_B + {}^G \boldsymbol{\epsilon}_B \times {}^G \mathbf{R} \left({}^B \boldsymbol{f}_j + {}^B \boldsymbol{h}_j \right) + {}^G \boldsymbol{\omega}_B \times \left({}^G \boldsymbol{\omega}_B \times {}^G \mathbf{R} \right) \left({}^B \boldsymbol{f}_j + {}^B \boldsymbol{h}_j \right) + {}^G \boldsymbol{\omega}_B \times {}^G \mathbf{R} \left({}^B \boldsymbol{\nu}_{F_j} + {}^B \boldsymbol{h}_j \right) + {}^H_j \mathbf{R}^{H_j} \mathbf{a}_{F_j} + {}^G \boldsymbol{\omega}_B \times {}^G \mathbf{R}^B \boldsymbol{\nu}_{F_j} \\ {}^G \boldsymbol{\epsilon}_{F_j} = {}^G \boldsymbol{\epsilon}_B + {}^H_j \mathbf{R}^{H_j} \boldsymbol{\epsilon}_{F_j} + {}^G \boldsymbol{\omega}_B \times {}^G \mathbf{R}^B \boldsymbol{\omega}_{F_j} \end{cases} \quad (14)$$

Writing Eq. (14) into the matrix form as

$$\begin{aligned} {}^G \ddot{\mathbf{X}}_{F_j} &= {}^G_{F_j} \mathbf{J}^{-1} {}^G \ddot{\mathbf{X}}_B + {}^G_{H_j} \tilde{\mathbf{R}}^{H_j} \ddot{\mathbf{X}}_{F_j} + {}^G \tilde{\boldsymbol{\omega}}_B \times {}^G_{H_j} \tilde{\mathbf{R}}^{H_j} \dot{\mathbf{X}}_{F_j} + {}^G \dot{\mathbf{q}}_B {}^B \tilde{\boldsymbol{f}}_j \\ \Rightarrow {}^G \ddot{\mathbf{X}}_B &= {}^G \mathbf{J}_{L_j} \ddot{\mathbf{q}}_{L_j} + \dot{\mathbf{q}}_{L_j}^T {}^G \mathbf{H}_L \dot{\mathbf{q}}_{L_j} + {}^G \dot{\mathbf{q}}_B {}^B \tilde{\boldsymbol{f}}_j + {}^{GH} \mathbf{J}_{L_j} \dot{\mathbf{q}}_{L_j} + {}^G_{F_j} \mathbf{J}^G \ddot{\mathbf{X}}_{F_j} \end{aligned} \quad (15)$$

where

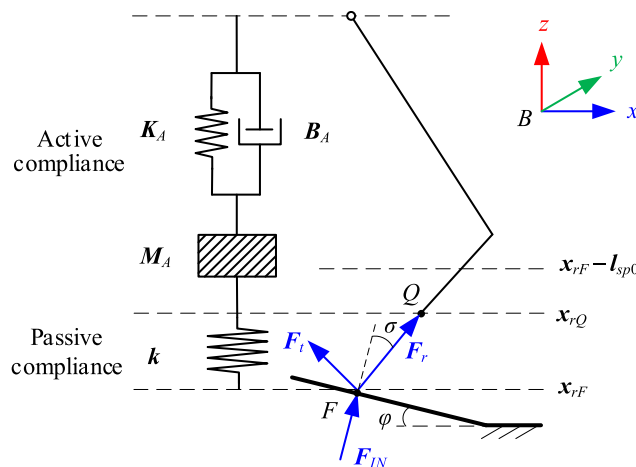


Fig. 4. Equivalent model of active and passive compliance.

$$\begin{aligned} {}^G\tilde{\boldsymbol{\omega}}_B &= \begin{bmatrix} 2{}^G\boldsymbol{\omega}_B & \mathbf{0} \\ \mathbf{0} & {}^G\boldsymbol{\omega}_B \end{bmatrix}, {}^H_j\tilde{\mathbf{R}} = \begin{bmatrix} {}^B_R^B \mathbf{R} & \mathbf{0} \\ \mathbf{0} & {}^B_R^B \mathbf{R} \end{bmatrix}, {}^G\mathbf{H}_L = {}^G_{F_j}J_{H_j}^G \tilde{\mathbf{R}} \otimes {}^{H_j}\mathbf{H}_L \\ {}^B\tilde{\mathbf{f}}_j &= \begin{bmatrix} {}^B\mathbf{f}_j + {}^B\mathbf{h}_j \\ {}^B\mathbf{h}_j \end{bmatrix}, {}^G\dot{\tilde{\mathbf{q}}}_B = \begin{bmatrix} {}^G\boldsymbol{\omega}_B \times \left({}^G\boldsymbol{\omega}_B \times {}^G_{H_j}\mathbf{R} \right) & {}^G\boldsymbol{\omega}_B \times {}^G_{H_j}\mathbf{R} \\ \mathbf{0} & \mathbf{0} \end{bmatrix} \end{aligned}$$

For the whole system, the acceleration equation is written as

$${}^B\mathbf{J}_I {}^G\ddot{\mathbf{X}}_B = {}^G\mathbf{J}_B \ddot{\mathbf{q}}_B + \dot{\mathbf{q}}_B^T {}^G\mathbf{H}_B \dot{\mathbf{q}}_B + {}^G\tilde{\mathbf{q}}_B {}^B\tilde{\mathbf{f}} + {}^{GH}\mathbf{J}_B \dot{\mathbf{q}}_B + {}_F^G\mathbf{J}^G \ddot{\mathbf{X}}_F \quad (16)$$

If the wheel is in complete contact with the ground with no slippage, then ${}^G\ddot{\mathbf{X}}_F = \mathbf{0}$.

3. Performance analysis of passive and active compliance

3.1. Equivalent stiffness and deformation capability

Impedance control regulates interaction forces by adjusting the impedance of the system, enabling it to behave like a virtual mechanical spring and damper in response to external stimuli. Due to the series-parallel hybrid structure of each leg, and the target impedance effects manifested at the end effector, impedance control is implemented in the Cartesian task space. Separate each leg from point Q , with the upper part being the actively compliant section, and the lower part being the passively compliant section. Each leg is compliant only in the x -axis and z -axis. The active and passive compliance system model is shown in Fig. 4. All the following vectors are represented in the body coordinate system $\{B\}$. For simplicity, the top left corner label is omitted. The position vectors of point Q and point F are denoted as \mathbf{x}_{rQ} and \mathbf{x}_{rF} , respectively. \mathbf{F}_{IN} is the ground reaction force. \mathbf{F}_r is the reaction force along the direction of spring compression, which is the actual contact force of point Q . \mathbf{F}_d is the desired contact force. \mathbf{x}_{rQ} and \mathbf{x}_{dQ} are the actual position and desired position of point Q , respectively. $\delta_x = \mathbf{x}_{rQ} - \mathbf{x}_{dQ}$, $\delta_F = \mathbf{F}_d - \mathbf{F}_r$. Expressed through passive springs, the actual position of point Q is given by

$$\mathbf{x}_{rQ} = \mathbf{x}_{rF} - \left(\mathbf{l}_{sp0} - \frac{\mathbf{F}_r}{k} \right) \quad (17)$$

where \mathbf{x}_{rF} is the actual position vector of point F . During exploration, the desired force is set to be constant, therefore, let $\dot{\mathbf{F}}_d = \ddot{\mathbf{F}}_d = \mathbf{0}$. When the system is in stable contact with the environment, let the desired acceleration of the leg in the body frame $\{B\}$ be constant, which means $\ddot{\mathbf{x}}_{dQ} = \dot{\mathbf{x}}_{dQ} = \mathbf{0}$, $\delta\ddot{\mathbf{F}} = \delta\dot{\mathbf{F}} = \mathbf{0}$. Substituting Eq. (17) into the dynamics equation of impedance control, the deviation of the force satisfies

$$\delta\mathbf{F} = \mathbf{k}_{eq} \left(\mathbf{x}_{rF} - \mathbf{l}_{sp0} - \mathbf{x}_{dQ} + \frac{\mathbf{F}_d}{k} \right) = \mathbf{k}_{eq} (\mathbf{x}_{rF} - \mathbf{x}_{dQ}) \quad (18)$$

where \mathbf{k}_{eq} is the equivalent stiffness. It represents the resistance of the system to external forces at the end-effector. Since the equivalent stiffness along the x -axis and the z -axis is equal, k_{eq} is expressed as

$$\mathbf{k}_{eq} = \frac{k\mathbf{K}_A}{k + \mathbf{K}_A} \quad (19)$$

The unit displacement of the foot end-effector F is denoted as δ_f , $\mathbf{f} = [x, y, z, \alpha, \beta, \gamma]^T$. The relationship between external disturbance $\delta\mathcal{F}_{IN}$ and the end-effector center displacement satisfies

$$\delta\mathcal{F}_{IN} = \begin{bmatrix} \delta\mathbf{F}_{IN} \\ \delta\mathbf{T}_{IN} \end{bmatrix} = \begin{bmatrix} \mathbf{K}_f & \mathbf{K}_c \\ \mathbf{K}_c^T & \mathbf{K}_t \end{bmatrix} \delta\mathbf{f} = \mathbf{K}_P \delta\mathbf{f} \quad (20)$$

where \mathbf{K}_f and \mathbf{K}_t are translational stiffness and rotational stiffness, respectively. \mathbf{K}_c is coupling stiffness. Here it is a zero matrix. \mathbf{K}_P is a symmetric positive semi-definite matrix, defined as the stiffness matrix.

For the elements x and y in the vector \mathbf{f} , the end-effector exhibits compliant spring characteristics with large deformation, thus joint deformation can be disregarded. The angle between the input force \mathbf{F}_{IN} and the direction vector of the calf is denoted as σ . It can be calculated from $\sigma = \pi/2 + \varphi - \beta$, where φ is the angle of the slop, β is the Euler angle of the end-effector. The contact force of point Q and the input torque acting on the body are written as

$$\delta\mathbf{F}_{IN} = \delta\mathbf{F}_r / \cos\sigma \quad (21)$$

For the elements α , β , γ and y in the vector \mathbf{f} , only joint deformations are considered. For the system, the input joint force vector is τ . The force Jacobian $\tilde{\mathbf{J}}$ is defined as

$$\mathcal{F} = \begin{bmatrix} \mathbf{F} \\ \mathbf{T} \end{bmatrix} = \tilde{\mathbf{J}}\tau = \begin{bmatrix} \tilde{\mathbf{J}}_F \\ \tilde{\mathbf{J}}_T \end{bmatrix} \tau \quad (22)$$

According to the principle of virtual work, the relationship between force Jacobian $\tilde{\mathbf{J}}$ and velocity Jacobian \mathbf{J} can be deduced from $\tilde{\mathbf{J}} = (\mathbf{J}^T)^{+1}$. The relationship between joint deformation and corresponding joint torque satisfies

$$\delta\boldsymbol{\tau} = \mathbf{K}_J \delta\mathbf{q}, \mathbf{K}_J = \text{diag}(k_{J1}, k_{J2} \dots k_{Jm})^T \quad (23)$$

where m is the number of the driving joints. k_{ji} represents the stiffness of driver i , $i = 1 \dots m$. Assuming all joints have the same stiffness, which means that $k_{ji} = k_J$. The end-effector displacement $\delta\mathbf{f}$ caused by joint deformation can be expressed by

$$\delta\mathcal{F}_{IN} = \frac{1}{\cos\sigma} (\mathbf{J}_L \mathbf{K}_J^{-1} \mathbf{J}_L^T)^{+1} \delta\mathbf{f} \quad (24)$$

Therefore, the stiffness matrix caused by joint deformations satisfies

$$\mathbf{K}_q = \frac{1}{\cos\sigma} (\mathbf{J}_L \mathbf{K}_J^{-1} \mathbf{J}_L^T)^{+1} \quad (25)$$

The elements on the diagonal of matrix \mathbf{K}_q are denoted as $[k_{q1}, k_{q2} \dots k_{q6}]$. According to the analysis above, when subjected to external disturbance, the stiffness matrices of each leg are expressed as

$$\begin{cases} \mathbf{K}_f = \text{diag}\left(\frac{k_{eq}}{\cos\sigma}, k_{q2}, \frac{k_{eq}}{\cos\sigma}\right) \\ \mathbf{K}_t = \text{diag}(k_{q4}, k_{q5}, k_{q6}) \end{cases} \quad (26)$$

The translation displacement deformation $\delta\mathbf{f}_T$ and angular displacement deformation $\delta\mathbf{f}_R$ of the end-effector can be represented separately as

$$\begin{bmatrix} \delta\mathbf{f}_T \\ \delta\mathbf{f}_R \end{bmatrix} = \mathbf{K}_P^{-1} \mathcal{F}_E = \begin{bmatrix} \mathbf{S}_T \mathcal{F}_E \\ \mathbf{S}_R \mathcal{F}_E \end{bmatrix} \quad (27)$$

The eigenvectors of matrices \mathbf{S}_T and \mathbf{S}_R are $\lambda_{S_T} = [\lambda_{S_{Tx}} \quad \lambda_{S_{Ty}} \quad \lambda_{S_{Tz}}]^T$ and $\lambda_{S_R} = [\lambda_{S_{Rx}} \quad \lambda_{S_{Ry}} \quad \lambda_{S_{Rz}}]^T$, respectively. The translation deformation coefficient on the z -axis is defined as the square root of the corresponding component within the eigenvector, and the rotation deformation coefficient around y -axis is defined as the square root of the corresponding components within the eigenvector. They are written as

$$\eta_{S_{Tz}} = \sqrt{\lambda_{S_{Tz}}}, \eta_{S_{Ry}} = \sqrt{\lambda_{S_{Ry}}} \quad (28)$$

3.2. Load capacity

When considering the maximum load capacity of the system, assume that the passive spring has already been triggered. In Fig. 5, there are two springs with stiffness values of k_1 and k_2 , respectively. Each spring has a fixed length under the same exerting force, leading to a circle of all possible positions for point Q . For the same stiffness spring, each point Q on the circle corresponds to a possible configuration due to the influence of the active joints. The joint configuration after terrain adaption could be determined by the active

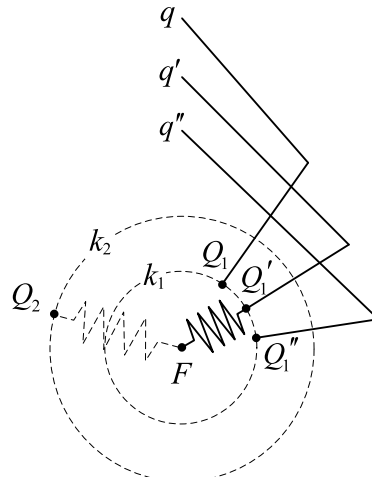


Fig. 5. System configuration with different spring stiffness.

compliance stiffness parameter K_A .

To ensure the effectiveness of the spring, the maximum force exerted at the end should be less than its maximum working load, denoted as $F_{sp\max}$. The direction of $F_{sp\max}$ is along the direction of spring compression. When $F_{sp\max}$ is applied to the end of the spring, the system satisfies

$$\mathbf{F}_{sp\max} = [\tilde{\mathbf{J}}_F]_{sp\max} \boldsymbol{\tau}_{sp\max} \quad (29)$$

The eigenvector of the matrix $[\tilde{\mathbf{J}}_F]_{sp\max}$ is denoted as $\lambda_{sp\max}$, with the value on the z -axis component denoted as $\lambda_{sp\max z}$. The eigenvectors of matrices $\tilde{\mathbf{J}}_F$ and $\tilde{\mathbf{J}}_T$ are λ_F and λ_T , respectively. When the contact surface is hard and frictional, the system force capacity coefficient along the z -axis is defined as the minimum value between the spring capacity and the joint capacity. The system torque capacity coefficient along the y -axis is defined as the square root of the component in the y -axis direction within the eigenvector. They are expressed as

$$\eta_{C_{F_z}} = \min\left(\sqrt{\lambda_{sp\max z}}, \sqrt{\lambda_{F_z}}\right), \eta_{C_{T_y}} = \sqrt{\lambda_{T_y}} \quad (30)$$

3.3. Compliance energy distribution

Due to the external disturbances, external energy is imparted to the leg. The external energy is absorbed by the spring and impedance control algorithm, which is regarded as the passive compliance energy, ΔE_P , and active compliance energy, ΔE_A , respectively. They are written as

$$\begin{cases} \Delta E_P = \frac{1}{2} k (l_{sp}^2 - l_{sp'}^2) \\ \Delta E_A = \int_0^N \sum_{j=1}^5 \Delta \tau_j \Delta \theta_j \end{cases} \quad (31)$$

where N is the number of interval segments from the initial state to the terminal state. τ is the torque of the driven joint.

The index of Active Compliance Energy (ACE) distribution coefficient is defined as

$$\eta_{ACE} = \frac{\Delta E_A}{\Delta E_P + \Delta E_A} \quad (32)$$

In Fig. 6, two different scenarios of active and passive compliance energy distribution are presented. Scenario (a) refers to when the system is in the initial state. After adjusting the suspension system, scenario (c) corresponds to a larger η_{ACE} value compared to scenario (b).

The length of the spring while moving in a standard posture is l_{sp} , and after driving on the slope, the length becomes $l_{sp'}$. Therefore, the energy absorbed by the passive compliance is

$$\Delta E_P = \frac{1}{2} k (l_{sp}^2 - l_{sp'}^2) \quad (33)$$

Active compliance energy is considered as mechanical work done by all the active joint motors. When the rover is driving in the standard posture, its initial joint configurations are denoted as $\theta_{j0}, j = 1 \dots 4$. Joint torques are denoted as $\tau_{j0}, j = 1 \dots 4$. After suspension adjustment, joint configurations and joint torques change into θ'_j and τ_j , respectively. Therefore,

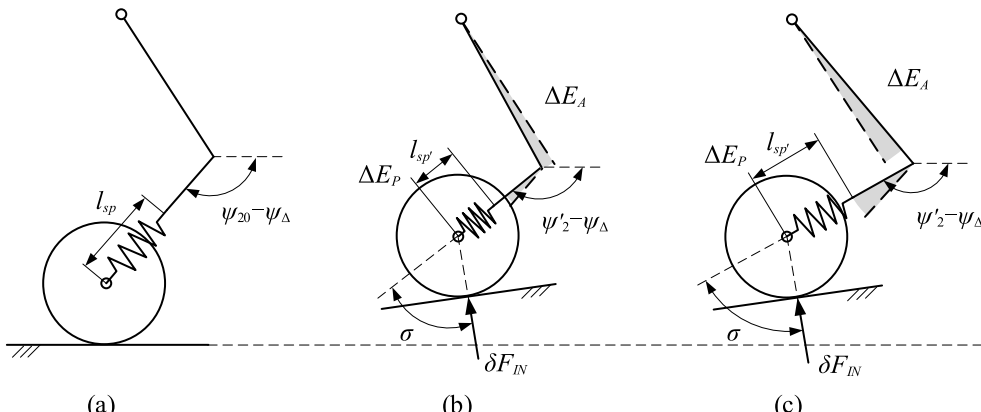


Fig. 6. Schematic diagram of active and passive compliance energy distribution.

$$\begin{cases} \Delta\tau_j = \tau_{j,n+1} - \tau_{j,n}, \tau_{j,0} = \tau_{j0}, \tau_{j,N} = \tau_j, 0 \leq n \leq N-1 \\ \Delta\theta_j = \theta_{j,n+1} - \theta_{j,n}, \theta_{j,0} = \theta_{j0}, \theta_{j,N} = \theta_j \end{cases} \quad (34)$$

By substituting Eqs. (33) and (34) into Eq. (31), the energy absorbed by passive and active compliance can be obtained separately.

3.4. System dynamic stability

The primary focus to evaluate the stability margin of a ground rover system is typically on ensuring the stability of the central body. In the situation discussed in this paper, the rover consistently maintains all wheels on the ground. However, influenced by the compliance strategy, the support polygon formed by the contact points and the body height varies, which means that the degree of stability is variable. The diagram of the support polygon and stability analysis are shown in Fig. 7. The force analysis of the rover during driving is shown in subfigure (a). Subfigure (b) is a simplified schematic diagram for force and position analysis.

The torque exerted on the supporting edge is represented as T_{sm} , $m = 1 \dots 4$. When the torque is positive, it is denoted as T_{sm}^+ , indicating that this torque contributes positively to stabilizing the rover. When the torque is negative, it is denoted as T_{sm}^- , indicating that this torque would lead to a tipover along the supporting edge. When the torque equals 0, it is the critical value. The position vector of the supporting points in the ground coordinate system $\{G\}$ is denoted as ${}^G p_m$, $m = 1 \dots 4$. According to the kinematic modeling, the position vector of the end-effector ${}^H f_m$ could be obtained. r_m is the position vector from the wheel center to the contact point. All the following vectors are represented in the ground coordinate system $\{G\}$. For simplicity, the top left corner label is omitted.

The vector of the supporting edge is denoted as l_m , and its unit vector is denoted as \hat{l}_m . It can be obtained from

$$\begin{cases} \hat{l}_m = \frac{{}^G p_{m-1} - {}^G p_m}{\| {}^G p_{m-1} - {}^G p_m \|}, m > 1 \\ \hat{l}_m = \frac{{}^G p_4 - {}^G p_m}{\| {}^G p_4 - {}^G p_m \|}, m = 1 \end{cases} \quad (35)$$

The force and torque acting on the link l_{ij} , $i = 1 \dots 4$, $j = 1 \dots 6$, are denoted as F_{lij} and T_{lij} , respectively. The ground reaction force and torque acting on the foot end-effector i are denoted as F_{ri} and T_{ti} . The force and torque acting on the body are denoted as F_B and T_B , respectively. The external force and torque acting on the body are denoted as F_E and T_E , respectively. They are generated by the gravitational force and inertia force of the load. The whole system is in a state of dynamic equilibrium under the influences of gravity, inertia, external force, and ground reaction forces. The equilibrium equations are written as

$$\begin{cases} \sum_{i=1}^4 \sum_{j=1}^6 F_{lij} + F_B + F_E + \sum_{i=1}^4 T_{ri} = 0 \\ \sum_{i=1}^4 \sum_{j=1}^6 T_{lij} + T_B + T_E + \sum_{i=1}^4 T_{ti} = 0 \end{cases} \quad (36)$$

The torque exerted by the link l_{ij} on the supporting point p_m can be expressed as

$$m T_{lij} = (\mathbf{r}_{lij} - \mathbf{p}_m) \times m_{lij} (\mathbf{g} - \dot{\mathbf{v}}_{lij}) + I_{0lij} \dot{\omega}_{lij} + \omega_{lij} \times (I_{0lij} \omega_{lij}) \quad (37)$$

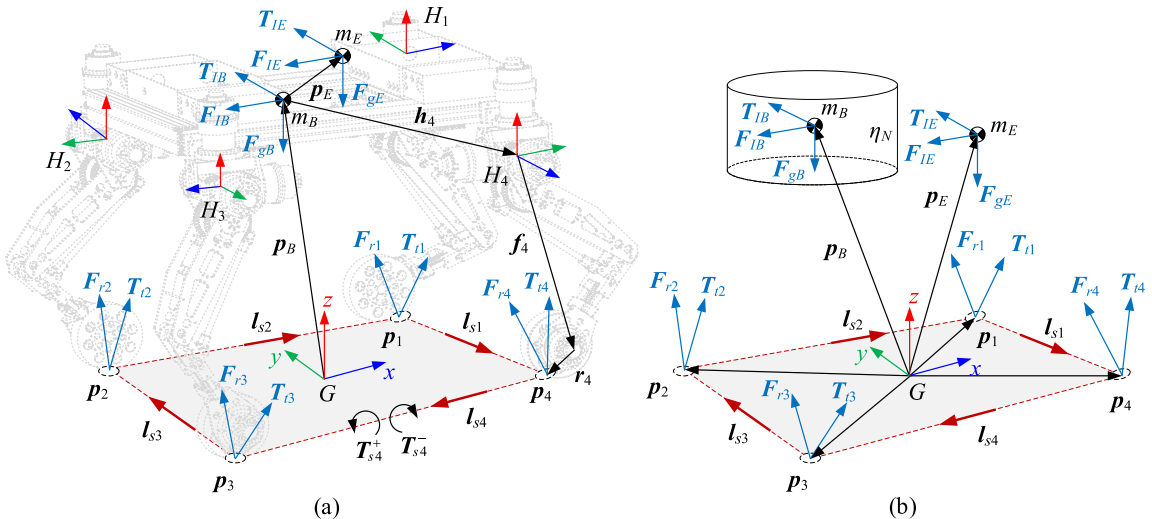


Fig. 7. Support polygon and stability analysis.

where \mathbf{r}_{lij} is the position vector of the CoM of link l_{ij} , \mathbf{v}_{lij} and $\boldsymbol{\omega}_{lij}$ are linear velocity and angular velocity of the CoM, respectively.

The torques exerted by the body and the load on the supporting point p_m can be expressed as

$$\begin{cases} {}^m\mathbf{T}_B = (\mathbf{p}_B - \mathbf{p}_m) \times m_B(\mathbf{g} - \dot{\mathbf{v}}_B) + \mathbf{I}_{0B}\dot{\boldsymbol{\omega}}_B + \boldsymbol{\omega}_B \times (\mathbf{I}_{0B}\boldsymbol{\omega}_B) \\ {}^m\mathbf{T}_E = (\mathbf{p}_E - \mathbf{p}_m) \times m_E(\mathbf{g} - \dot{\mathbf{v}}_E) + \mathbf{I}_{0E}\dot{\boldsymbol{\omega}}_E + \boldsymbol{\omega}_E \times (\mathbf{I}_{0E}\boldsymbol{\omega}_E) \end{cases} \quad (38)$$

where m_E is the mass of the load, \mathbf{v}_E and $\boldsymbol{\omega}_E$ are its linear velocity and angular velocity, respectively. Since the load is fixed on the body, the angular velocity of the load is equal to the angular velocity of the body, which is $\boldsymbol{\omega}_E = \boldsymbol{\omega}_B$. According to the principle of velocity synthesis, $\mathbf{v}_E = \mathbf{v}_B + \boldsymbol{\omega}_B \times (\mathbf{p}_E - \mathbf{p}_B)$. \mathbf{p}_E is the position vector of the CoM of the load in frame $\{G\}$. \mathbf{p}_B is the position vector of the CoM of the body.

The combined torque at supporting point p_m is generated by reaction forces from other supporting points \mathbf{F}_n , the torque exerted by the body ${}^m\mathbf{T}_B$, the torque exerted by the load ${}^m\mathbf{T}_E$, and the torque exerted by links. It is written as

$$\mathbf{T}_{pm} = \sum_{i=1}^4 \sum_{j=1}^5 {}^m\mathbf{T}_{lj} + {}^m\mathbf{T}_B + {}^m\mathbf{T}_E + \sum_{n=1}^4 (\mathbf{p}_m - \mathbf{p}_n) \times \mathbf{F}_n, n \neq m \quad (39)$$

The combined torque about the supporting edge l_m is equal to the projection of torque acting on the supporting point onto the edge vector. Therefore, the combined torque about the supporting edge l_m is expressed as

$$\mathbf{T}_{sm} = \mathbf{T}_{pm} \cdot \hat{\mathbf{l}}_m = \sum_{i=1}^4 \sum_{j=1}^5 {}^m\mathbf{T}_{lj} \cdot \hat{\mathbf{l}}_m + {}^m\mathbf{T}_B \cdot \hat{\mathbf{l}}_m + {}^m\mathbf{T}_E \cdot \hat{\mathbf{l}}_m + \sum_{n=1}^4 (\mathbf{p}_m - \mathbf{p}_n) \times \mathbf{F}_n \cdot \hat{\mathbf{l}}_m, n \neq m \quad (40)$$

The definition of the stability margin for tipover around support edge l_m is denoted as

$$\eta_{Nm} = \text{sgn}(\mathbf{T}_{sm}) \frac{\|\mathbf{T}_{sm}\|}{\|\mathbf{T}_{\text{standard}}\|} \quad (41)$$

where $\text{sgn}(\cdot)$ stands for the sign function.

The $\mathbf{T}_{\text{standard}}$ is the combined torque about the supporting edge l_m in standard posture, where the rover drives at a constant velocity, the supporting polygon is a square, and the projection of the CoM of the body is located at the diagonal intersection point. For the whole system, the system stability coefficient is defined as the minimum value of all supporting edges,

$$\eta_N = \min(\eta_{Nm}), m = 1 \dots 4 \quad (42)$$

During the driving of the rover, the stability coefficient should be greater than the minimum threshold to ensure safety, which is $\eta_{N\min} \leq \eta_N$.

4. Performance optimization and parameters design

4.1. Optimization approach and parameters

Considering that the performance atlas method allows for quicker convergence towards optimal or near-optimal solutions and facilitates informed decision-making in multi-objective optimization problems, it is chosen to solve the performance optimization problem. This paper aims to obtain the optimal stiffness of the rover during driving, including the stiffness of the active compliance control algorithm K_A and the passive compliance spring k , as they influence the rover's response to external forces and its ability to maintain stable postures. The standard driving posture of the rover on flat terrain is considered the initial state. After being subjected to external forces from the terrain and adjusted to a stable state, the posture is regarded as the final state. The stiffness of the active and passive parts determines the overall performance of the system, which is reflected in the final posture. When the system is in a stable state after terrain adaption, active compliance stiffness can be reflected in the active joint displacement, and passive compliance stiffness can be reflected in the spring length variation. The relationship between active compliance stiffness K_A and the position of point Q can be obtained from the system stiffness model. With the position of point Q , the driven joints' position can be calculated from the kinematic model. Since only joint 3 and joint 4 play a regulating role in each leg, K_A can be represented by θ_3 and θ_4 . Therefore, the optimization parameters are the passive spring stiffness k , and the driven joint positions θ_3 and θ_4 .

4.2. Constraint conditions

The optimization process considers several constraints to ensure the practical feasibility of the solutions, mainly including the motion range constraints and the spring compression limits. The driven joints have motion range constraints due to the structural limitation, with the upper bound of $\theta_{3\max}$, $\theta_{4\max}$ and the lower bound of $\theta_{3\min}$, $\theta_{4\min}$. These are actually workspace constraints under kinematic geometry considerations, given by

$$\begin{cases} \theta_{3\min} \leq \theta_3 \leq \theta_{3\max} \\ \theta_{4\min} \leq \theta_4 \leq \theta_{4\max} \end{cases} \quad (43)$$

In addition, to ensure that the compression of the spring is within the working range, the stiffness of the spring needs to satisfy

$$0 \leq k \leq \frac{F_{G\max} \sin(\psi_{20} - \varepsilon)}{\mu \times 4 \times l_{sp0}} \quad (44)$$

where $F_{G\max}$ is the maximum load that the rover can carry (including its own weight). ψ_{20} refers to the joint ψ_2 when the rover is driving in a standard posture. μ is the load factor of the spring, it represents the minimum allowable compression deformation of the spring when the rover statically traverses by standard posture. Based on Eqs. (43) and (44), and taking empirical data into consideration, the limits of the design parameters are set within the ranges of $30^\circ \leq \theta_3 \leq 120^\circ$, $120^\circ \leq \theta_4 \leq 180^\circ$, and $0 \text{ N/mm} \leq k \leq 12 \text{ N/mm}$. When k equals 0, the system is rigid, and its stiffness is determined solely by the active compliance.

4.3. Performance indices

According to the analysis of Section 3, the deformation coefficient η_S , the active compliance energy η_{ACE} , the system stability η_N , and the system capacity η_C are utilized to find the optimal parameters. These indices serve as the optimization objectives, with the global optimum domain being the intersection of their individual optimum performance domains. These four performance indices are chosen as optimization objectives because they represent the key aspects of a rover's navigation: terrain compliance capability, energy efficiency, motion stability, and load capacity. To enhance compliance capability, it is preferable for the leg to have a large deformation in the z -axis direction. To enhance the motion precision, low deformation is preferred in the rotation direction. $\eta_{S_{Tz-\min}}$ refers to the minimum translation deformation coefficient of the system without external disturbances. $\eta_{S_{R_\beta-\max}}$ refers to the maximum acceptable deformation coefficient in the rotational direction to ensure the motion accuracy of the end effector. When performing tasks on extraterrestrial planets, energy is often extremely limited, therefore, η_{ACE} prefers to be minimized. In order to ensure safety, the system stability is set to be positive and greater than the minimum threshold $\eta_{N\min}$. The system load capacity should be larger than $F_{G\max}$ and is set to be as large as possible. $\eta_{C_{F_{G\max}}}$ and $\eta_{C_{T_{\max}}}$ refer to the force and torque capacity value when the rover is carrying the maximum load. In summary, the individual optimum performance domains are denoted as

$$\begin{cases} \Omega_S = \{(k, \theta_3, \theta_4) \mid \eta_{S_{Tz-\min}} \leq \eta_{S_{Tz}}, \eta_{S_{R_\beta}} \leq \eta_{S_{R_\beta-\max}}\} \\ \Omega_{ACE} = \{(k, \theta_3, \theta_4) \mid 0 \leq \eta_{ACE} \leq 1\} \\ \Omega_N = \{(k, \theta_3, \theta_4) \mid \eta_{N\min} \leq \eta_N\} \\ \Omega_C = \{(k, \theta_3, \theta_4) \mid \eta_{C_{F_{G\max}}} \leq \eta_{C_{F_z}}, \eta_{C_{T_{\max}}} \leq \eta_{C_{T_\beta}}\} \end{cases} \quad (45)$$

Taking the intersection of these individual indices domains, the global optimum domain is expressed as

$$\Omega_{GblOpt} = \Omega_S \cap \Omega_{ACE} \cap \Omega_N \cap \Omega_C \quad (46)$$

Optimal stiffness design aims to identify the global optimum region and determine the most suitable combination of stiffness parameters. By conducting a detailed analysis of each performance index and identifying its trend, the individual optimum performance domain can be determined. This domain represents the parameters where the specific performance is superior. The intersection of multiple performance domains forms the global optimum region. All parameters within this global optimum region exhibit superior

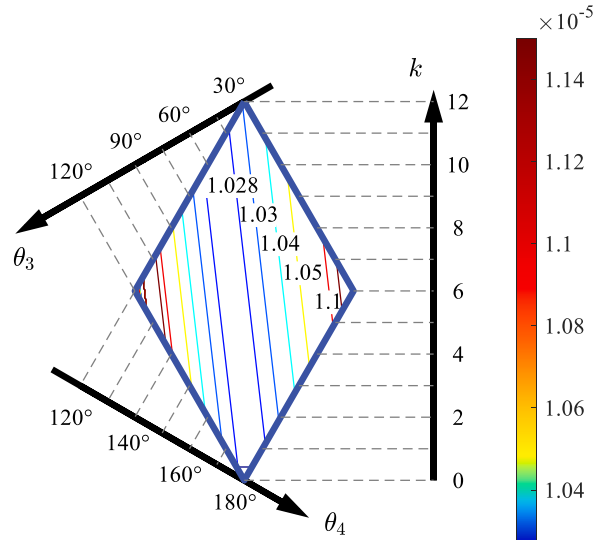


Fig. 8. The rotation deformation performance atlas.

comprehensive performance. Generally, the multi-objective optimal mechanism design problem does not have a unique solution. Overall, a better combination of optimization parameters generally leads to a better comprehensive terrain adaptive performance, typically resulting in larger η_N , η_{ST_z} , $\eta_{C_{F_2}}$, $\eta_{C_{T_p}}$, and smaller η_{ACE} , η_{SR_β} .

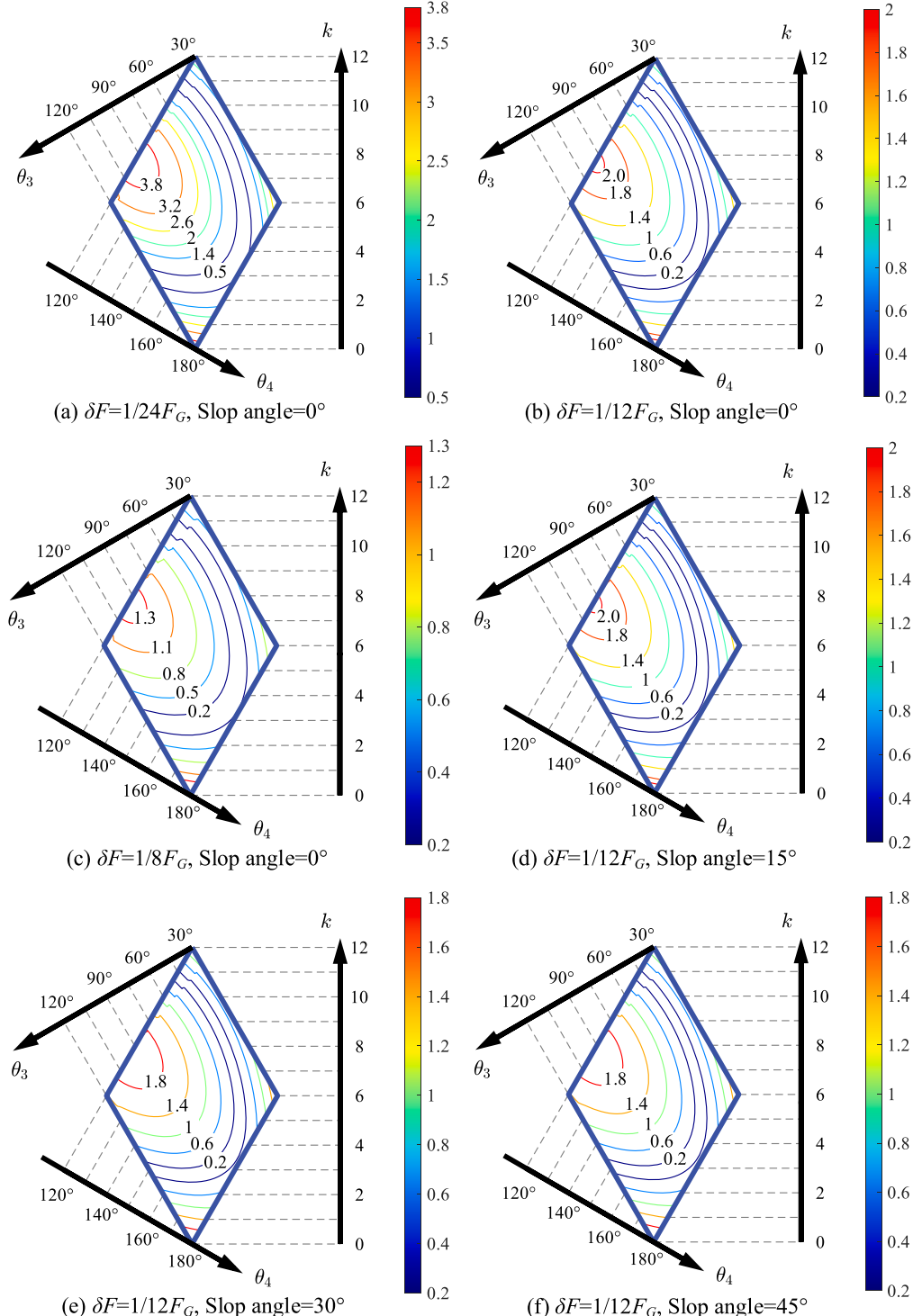


Fig. 9. The translation deformation performance atlases under different force deviation and slop angle.

5. Verifications

5.1. Deformation coefficient evaluation

The deformation coefficient is analyzed in this section. The force deviation at the end-effector is denoted as δ_F . θ_3 , θ_4 , and k are the three independent variables. In the analysis, the initial posture is the standard driving posture of the rover, with the overall gravitational force being F_G , $\theta_{30}=47.36^\circ$, $\theta_{40}=163.22^\circ$, $\psi_{20}=115.44^\circ$. The final posture is determined by θ_3 , θ_4 , and k . Worth noting that δ_F is perpendicular to the contact surface, and F_G is along the z -axis. The rover can achieve steering and hip abduction/adduction by the driven joints θ_1 and θ_2 , thereby enabling translation movement along the y -axis and rotational movement around the x -axis and the z -axis for the end-effector. However, since joints θ_1 and θ_2 do not provide terrain adaptability, their motion characteristics are no longer considered in this paper. Therefore, only $\eta_{S_{Tz}}$ and $\eta_{S_{R\beta}}$ are considered. They refer to the translation deformation coefficient on the z -axis and the rotation deformation coefficient around the y -axis, respectively.

Using the performance atlas method to display the relationship between the performance coefficient and the variables θ_3 , θ_4 , and k . The feasible ranges of the variables intersect to form a parallelogram. Each point within the parallelogram corresponds to a performance coefficient value, with contour lines indicating its value. The colors of the contours correspond to the values on the color bar, and the specific numerical values are marked on the diagrams. The rotation deformation coefficient is shown in Fig. 8. Here k_J is set to be 10^4 Nm/rad [34]. It can be seen that $\eta_{S_{R\beta}}$ is independent of the spring stiffness coefficient k and only related to the joint configuration of the system. In Fig. 9, performance atlases of the translation deformation coefficient are respectively shown under different δ_F values. It can be seen that the $\eta_{S_{Tz}}$ decreases with the increase of δ_F , but different values of δ_F correspond to the same trend in $\eta_{S_{Tz}}$. Subfigures (d)-(f) illustrate the impact of slope angle on the performance. Since the deviation of the ground reaction force δ_F is always perpendicular to the slope, the angle between the slope and the end-effector's Euler angle affects the force exerted on the spring. The comparison between subfigures (b) and (d)-(f) reveals that as the slope increases, $\eta_{S_{Tz}}$ decreases.

5.2. Load capacity evaluation

The load capacity is determined by the joint configuration and spring stiffness. Similar to Section 5.1, only $\eta_{C_{Fz}}$ and $\eta_{C_{T\beta}}$ are analyzed. The performance atlases are shown in Fig. 10. In subfigure (a), the atlas of the force load capacity on the z -axis is obtained from the eigenvector of the force Jacobian and the spring load capacity. It can be observed that the load capacity is determined by the minimum value between the maximum capacity provided by the joint configuration and the maximum capacity of the spring. Subfigure (b) shows the atlas of the maximum torque capacity around the y -axis. It can be seen that torque capacity is not affected by the spring stiffness.

5.3. Energy distribution evaluation

The ACE performance atlases with different force deviations and slope angles are shown in Fig. 11. The η_{ACE} reaches its minimum value when the joint configuration maintains the initial position. However, after external force interference, the joint configuration will not remain the same. Generally, a smaller variation in joint configuration corresponds to a smaller value of η_{ACE} . Additionally, as the force deviation increases, the value of η_{ACE} decreases. When the angle of the slope increases, η_{ACE} increases. This is because when

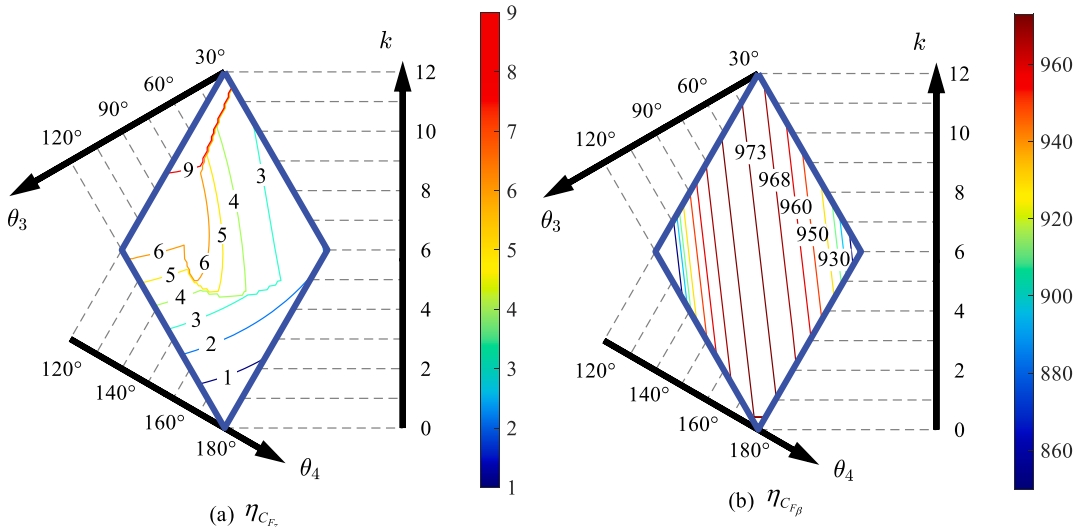


Fig. 10. The force and torque load capacity performance atlases.

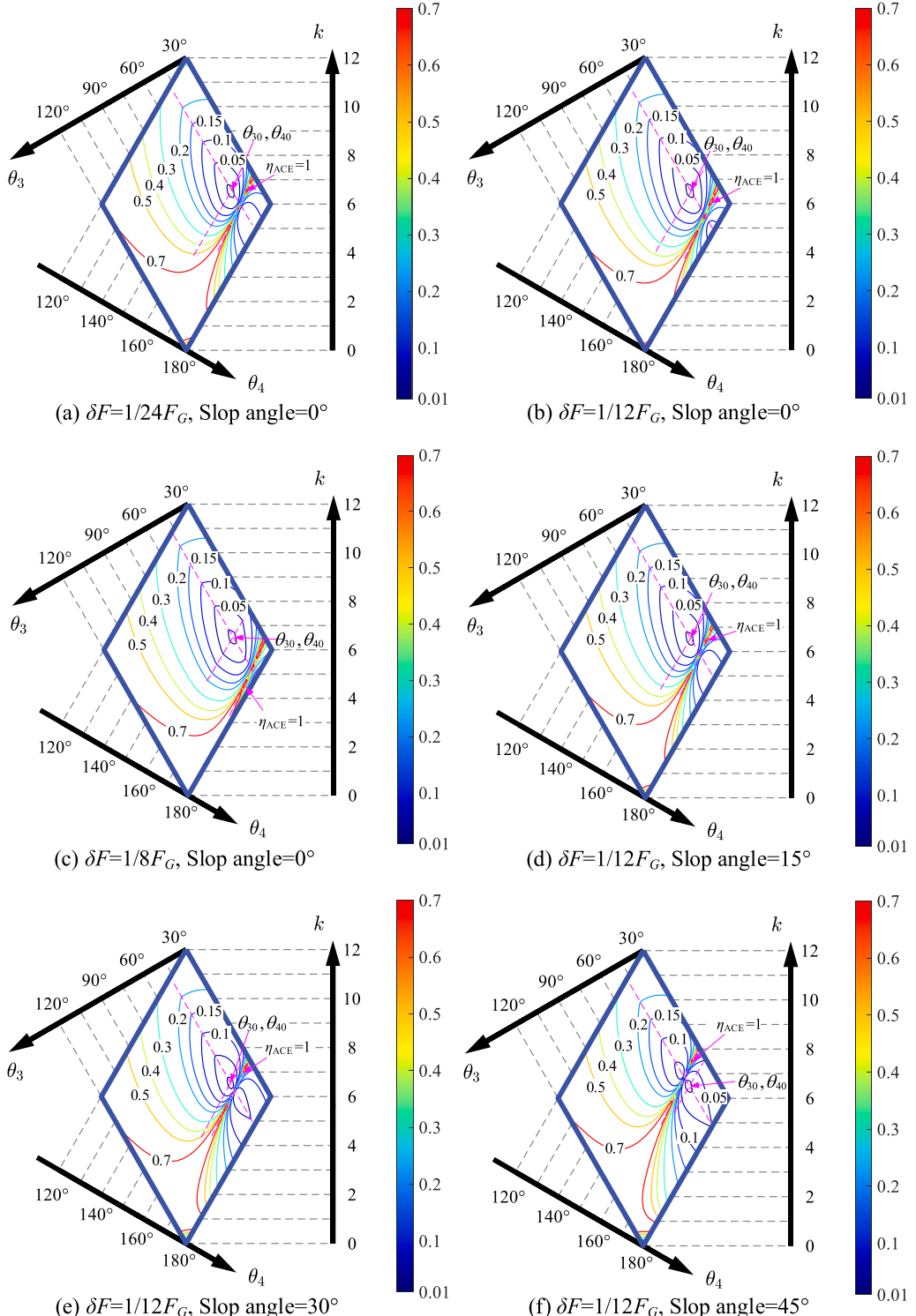


Fig. 11. The ACE distribution performance atlases under different force deviation and slop angle.

the system maintains the same posture, as the force deviation increases, more energy will be absorbed by the spring. When the external input force deviation remains constant, as the slop incline increases, the torque exerted on the system increases, while the supporting force decreases, resulting in an increase in η_{ACE} . Approximate symmetry axes exist in these atlases because the spring deformations are

the same before and after the adaptation process under these postures, which means $\eta_{ACE} = 1$. As the external force increases, the extension of the leg decreases, leading to a larger θ_4 . Consequently, the symmetric axis shifts in the positive direction of θ_4 as δ_F increases. Similarly, when the slope angle exists, the symmetric axis shifts in the negative direction of θ_4 to reach the $\eta_{ACE} = 1$ postures. Generally, for the same posture, a larger spring stiffness coefficient k corresponds to a smaller η_{ACE} . When k is equal, larger values of $|\Delta\theta_3|=|\theta_{30}-\theta_3|$ and $|\Delta\theta_4|=|\theta_{40}-\theta_4|$ correspond to a larger η_{ACE} .

5.4. Stability evaluation

When leg m encounters a slope and is disturbed by force variation, after the suspension system adapts to the terrain and becomes stable, the system stability evaluation index η_N is performed. In the analysis of system stability, all legs share the same compliance parameters. For the analysis of η_N , the body's position vector p_B , and the foot end-effector vector f_i , change with the varying of the parameters. The $T_{standard}$ is determined with the joint configurations $\theta_{i3}=\theta_{30}$, $\theta_{i4}=\theta_{40}$, $i=1\cdots 4$. Fig. 12 shows the relationship between η_N and the rover body's height. Δf_x refers to the displacement deviation of leg m 's end-effector on the x -axis from its initial value, with the initial value $f_{x0}=0$. $\Delta h_{bodyheight}$ represents the deviation in the rover's body height along the z -axis from the standard height. It can be observed that when the end-effector of leg m moves forward, resulting in an increase in the area of the supporting polygon, the stability of the system improves. However, if the end-effector moves along the negative x -axis, causing a decrease in the area of the supporting polygon, $\eta_N < 0$ implies that the system is unstable. η_{Nmin} is set to be the minimum stability margin. When $\Delta f_x=0$, η_N remains constant regardless of changes in the body height.

Fig. 13 shows the system stability performance atlases. In the atlases, smaller values of θ_3 and θ_4 lead to a larger displacement of the leg's end-effector in the positive direction along the x -axis, while larger values of θ_3 and θ_4 lead to a larger displacement in the negative direction along the x -axis. The results of the atlases are consistent with the results in Fig. 12. From subfigures (a) to (d), gradually increase the external force F_E acting on the rover's body. It can be seen that with the increase of F_E , the stability of the system relatively increases. During the early stage of the growth of F_E , η_N changes significantly. When F_E increases to a certain stage, the change in η_N is relatively small. It's worth noting that, regardless of the variation of F_E , the curve where $\eta_N=1$ remains unchanged. This is because when $\eta_N=1$, the combined torque on each supporting edge is the same as in the standard posture. These postures form the $\eta_N=1$ curve. Even if the external load acting on the body increases, these postures remain unaffected.

5.5. Optimum parameters selection and applicability verification

The individual performance indices are analyzed in the former sections. They provide evidence for comparing different performances and selecting the global optimum parameters. The purpose of selecting the inequality constraints that define the individual optimum performance domain is to ensure that the rover exhibits superior performance within this domain, and that the parameters satisfying these inequalities have an intersection. To standardize performance evaluation indices, a typical condition is selected for analysis, with $\delta_F=1/12F_G$, Slope angle=15°, and $F_E=1/3 F_G$. Based on the importance of individual coefficients, different levels of constraints can be applied. Based on Eq. (45), the individual performance domain is further refined. Their intersection constitutes the global optimum region and can be represented as

$$\Omega_{GblOpt} = \left\{ (k, \theta_3, \theta_4) \mid 0.95 \leq \eta_{S_{T_z}}, \eta_{S_{R_\beta}} \leq 1.05, 4 \leq \eta_{C_{F_z}}, 930 \leq \eta_{C_{T_\beta}}, \eta_{ACE} \leq 0.15, 0.95 \leq \eta_N \right\} \quad (47)$$

The global optimum region Ω_{GblOpt} is shown in Fig. 14. Theoretically, parameters within the global optimum region can all be

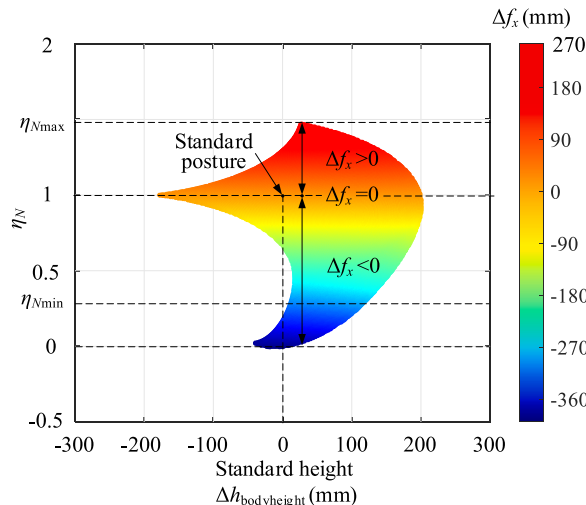


Fig. 12. The relationship between η_N and the body's height.

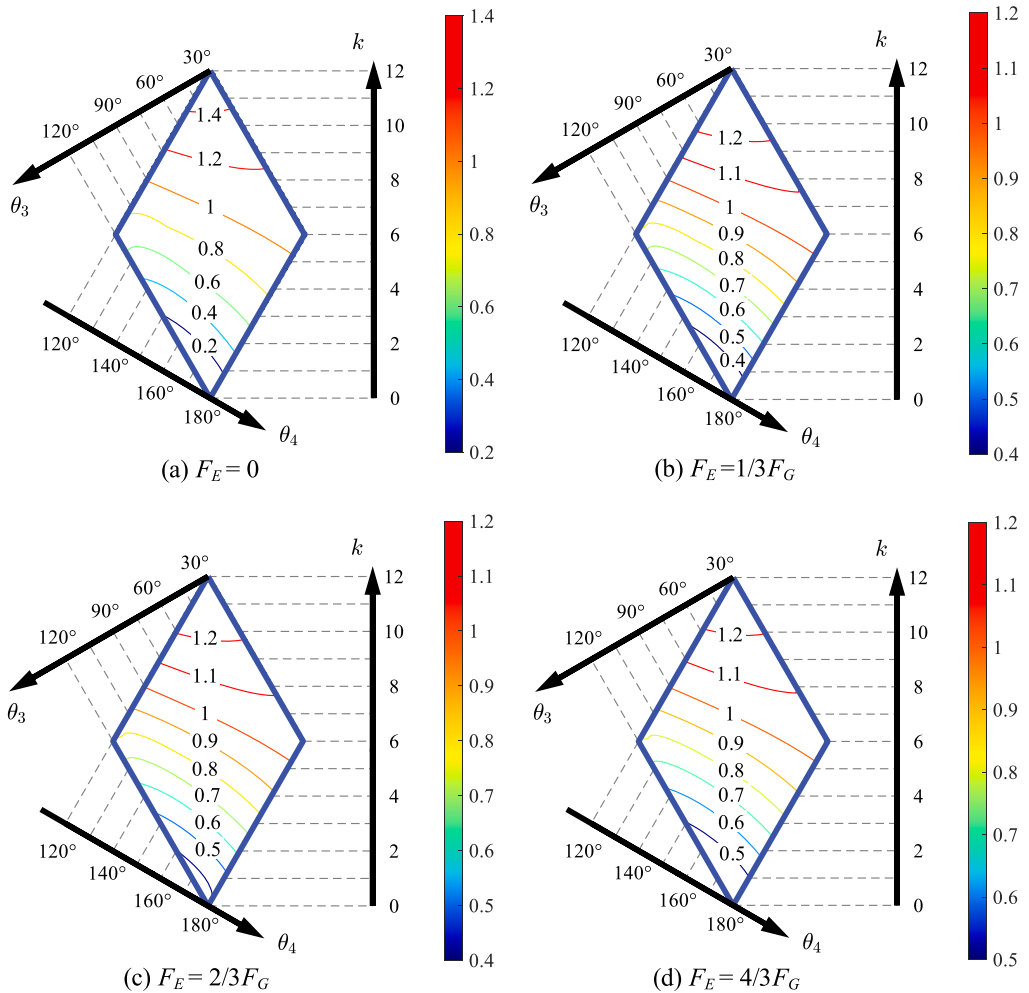


Fig. 13. The dynamic stability performance atlases under different load force.

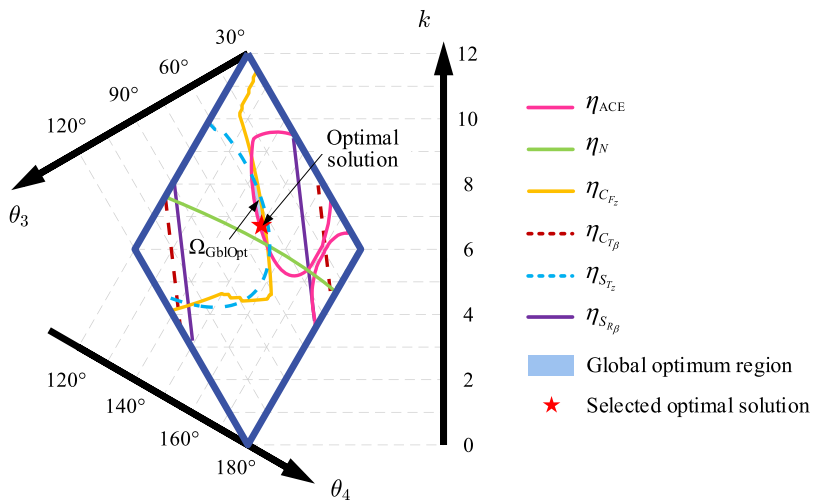


Fig. 14. The global optimum region and selected optimal solution for the rover.

considered feasible optimal solutions. The selected result is located in the middle of the region with $\eta_N = 1$, where the rover's body has the largest workspace. As a result, the selected numerical values for the optimum parameters combination (k, θ_3, θ_4) are (6.73 N/mm, 64.0°, 149.7°). According to the kinematic analysis, $K_A = 0.94$ N/mm. In order to verify that the designed stiffness combination (k, K_A) is suitable for all conditions, the performance indices are evaluated individually. The translation deformation coefficient can be calculated from Eqs. (19) and (28). It is related to the slope angle since the slope angle determines the component of support force along the spring compression axis. The rotation deformation coefficient is only related to the system's configuration. The condition for $\eta_{Sp_p} \leq 1.05$ to hold is that the driving joints satisfy the range constraints. So does the load capacity coefficient. From Section 5.4, it was shown that the curve where $\eta_N = 1$ remains unchanged regardless of the value of F_E . So there always exists an optimum parameter combination that can achieve $0.95 \leq \eta_N$ for any value of F_E .

5.6. Experiments

For comparative experiments, three springs with varying stiffness and different impedance control parameters are utilized, as shown in Fig. 15(a). Since it is unable to purchase a spring that perfectly matches the optimized stiffness, a substitute spring with a stiffness value close to the optimized result is utilized. Two different slopes are employed to validate the generality of optimization results, as shown in Fig. 15(b) and (c). The height h_1 of Terrain A is 20 cm, with a slope angle φ_1 of 30°. The height h_2 of Terrain B is 15 cm, with a slope angle φ_2 of 20°. On Terrain A, k is taken from 2.88, 5.06, and 10.60, and K_A is taken from 0.6, 0.8, ..., and 1.6. On Terrain B, k is taken from 2.88, 5.06, and 10.60, and K_A is taken from 0.8 to 1.0 near the optimal value. During the experiments, the initial state of the rover is its standard posture, as shown in Fig. 16(a). Next, it starts to drive forward and encounters the slope. The suspension system deforms to adapt to the terrain, with legs 1–3 stretching and leg 4 contracting, as depicted in Fig. 16(d). Adjusting the impedance control parameter K_A results in variations in leg length and body height, as shown in Fig. 16(b) and (c). Even with the same stiffness parameters, leg length and body height change when the terrain type varies, as illustrated in Fig. 16(e) and (f).

The results of the experiments conducted on Terrain A are shown in Fig. 17. Subfigures (a) and (b) respectively demonstrate the influence of K_A on the height of the body when k is consistent, and the influence of k on the height of the body when K_A is consistent. When K_A is larger, the deformation of the system due to external forces decreases, leading to a reduction in variation of the body height. Conversely, when K_A is smaller, the deformation of the system increases, resulting in the increase of the body height. As the spring is triggered, the passive spring stiffness can directly affect the height of the body. Moreover, greater stiffness in the passive spring corresponds to a larger change in body height. In subfigure (b), the concavity within the dashed box occurs because when the rover makes contact with the terrain, the spring rapidly contracts, leading to a sharp change in contact force, which in turn corresponds to a decrease in the height of the rover. Subfigures (c) and (d) respectively illustrate the impact of K_A when k remains constant, and the effect of k when K_A is held consistent on the pitch angle of the rover body's Euler angle. When K_A is small, the system undergoes large deformations in response to the same external interference force, resulting in increased body height and leg extension. When K_A equals 0.6, the extensions of legs 1, 2, and 3 reach their maximum limits, while leg 4 has not yet reached its maximum extension. Consequently, the body exhibits a greater pitch angle. Subfigures (e) and (f) illustrate the impact of K_A and k on the variation of system joint configuration, respectively. The results align with the body height variation, as a large variation in body height corresponds to a large variation in total joint configuration. Subfigures (g) and (h) illustrate the contact force deviation under different stiffness combinations. The contact force when the rover is driving in the standard posture is used as the comparison baseline and is set to 0. The results align with the trend of the pitch angle, where $K_A = 0.6$ exhibits a greater force deviation. When $K_A \geq 0.8$, the contact force deviations have similar values. When the spring stiffness is high, the deformation of the spring upon contact with the obstacle is small, resulting in a large peak contact force. Conversely, when the spring stiffness is low, the peak contact force is smaller due to greater spring deformation.

Fig. 18 shows the experiment results conducted on Terrain B. All the tests are carried out under $K_A = 1.0$. In subfigure (b), three of the gray dashed lines indicate the mean values of the curve during compliance. The comparison results from Terrains A and B reveals that all evaluation criteria exhibit the same trend. In subfigures (a) and (b), it is evident that a large terrain slope angle and slope height correspond to a large body height variation and a large total spring length variation. Since the body height variation increases, the total joint configuration variation increases accordingly, as shown in subfigure (c). In subfigure (d), the pitch angle increases as the slope angle and the slope height increase.

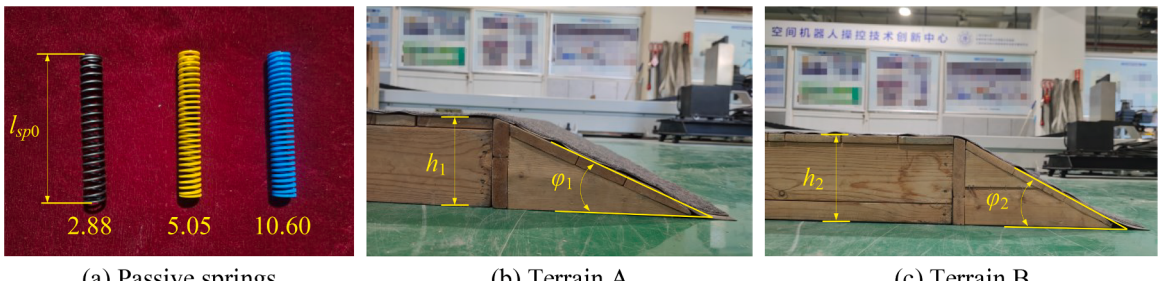


Fig. 15. The passive springs and terrains used in the experiments.

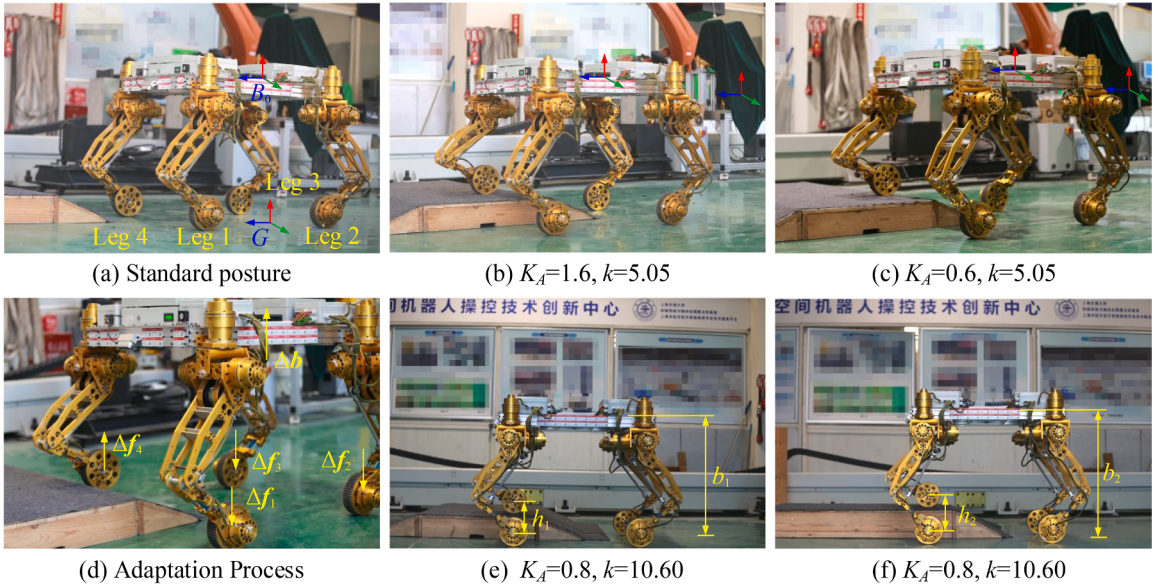


Fig. 16. Photos of the compliance effects during experiments.

The total time consumed during the compliance process is denoted as T . In order to evaluate the comprehensive performance of the system, the overall performance coefficient η_{ave} is defined as

$$\begin{aligned} \eta_{ave}(k, K_A) = & \frac{\int_0^T \eta_{S_{Tz}}(k, K_A, t) dt}{\int_0^T \eta_{S_{Tz-\max}} dt} + \frac{\int_0^T (\eta_{S_{R_\beta-\max}} - \eta_{S_{R_\beta}}(k, K_A, t)) dt}{\int_0^T \eta_{S_{R_\beta-\max}} dt} + \frac{\int_0^T \eta_{C_{Fz}}(k, K_A, t) dt}{\int_0^T \eta_{C_{Fz-\max}} dt} \\ & + \frac{\int_0^T \eta_{C_{T_\beta}}(k, K_A, t) dt}{\int_0^T \eta_{C_{T_\beta-\max}} dt} + \frac{\eta_{ACE_{\max}} - \eta_{ACE}(k, K_A, t)}{\eta_{ACE_{\max}}} + \frac{\int_0^T \eta_N(k, K_A, t) dt}{\int_0^T \eta_{N_{\max}} dt} \end{aligned} \quad (48)$$

This formula represents the proportions of average performance indices in their maximum capacity under different (k, K_A) combinations. A larger value of η_{ave} indicates that the system possesses greater overall performance capability. $\eta_{(\cdot)-\max}$ refers to the maximum value among all (k, K_A) pairs. Since the overall performance increases with the increase of $\eta_{S_{Tz}}$, $\eta_{C_{Fz}}$, $\eta_{C_{T_\beta}}$, and η_N , but decreases with the increase of both $\eta_{S_{R_\beta}}$ and η_{ACE} , $\eta_{S_{R_\beta}}$ and η_{ACE} are negative. Fig. 19 plots the numerical values of η_{ave} corresponding to different k and K_A under Terrain A. It can be seen that the stiffness combination (5.06, 1.0), which is closest to the designed stiffness, exhibits the best overall performance.

5.7. Algorithm comparisons

To better demonstrate the advantages of the performance atlas method in multi-objective optimization, it is compared with the interior-point optimization algorithm and multi-objective genetic algorithm. For the interior-point optimization algorithm, weighting factors are used to construct the objective function, transforming the multi-objective optimization problem into a single-objective optimization problem. The optimization equation can be expressed as

$$\begin{aligned} \max \xi(k, \theta_3, \theta_4) = & w_1 \frac{\eta_{S_{Tz}}}{\eta_{S_{Tz-\max}}} + w_2 \frac{\eta_{S_{R_\beta}}}{\eta_{S_{R_\beta-\max}}} + w_3 \frac{\eta_{ACE}}{\eta_{ACE_{\max}}} + w_4 \frac{\eta_N}{\eta_{N_{\max}}} + w_5 \frac{\eta_{C_{Fz}}}{\eta_{C_{Fz-\max}}} + w_6 \frac{\eta_{C_{T_\beta}}}{\eta_{C_{T_\beta-\max}}} \text{ s.t.} \\ & \begin{cases} 0 \leq k \leq k_{\max} \\ \theta_{3_{\min}} \leq \theta_3 \leq \theta_{4_{\min}} \\ \theta_{4_{\min}} \leq \theta_4 \leq \theta_{4_{\max}} \end{cases} \end{aligned} \quad (49)$$

where w_i ($i = 1 \cdots 6$) represents the weighting factor corresponding to each individual performance index.

The interior-point algorithm is applied to the objective function to solve for the optimal solution. Fig. 20(a) illustrates the feasible optimal solutions, along with their corresponding initial points and iteration processes. Initial points are randomly generated within the feasible region. The solution is considered to be successful if the obtained optimal solution falls within the global optimum region. It can be observed that the interior-point algorithm can get stuck in local optima of the optimization objective.

The multi-objective genetic algorithm aims to find Pareto optimal solutions by evolving a population of candidate solutions over

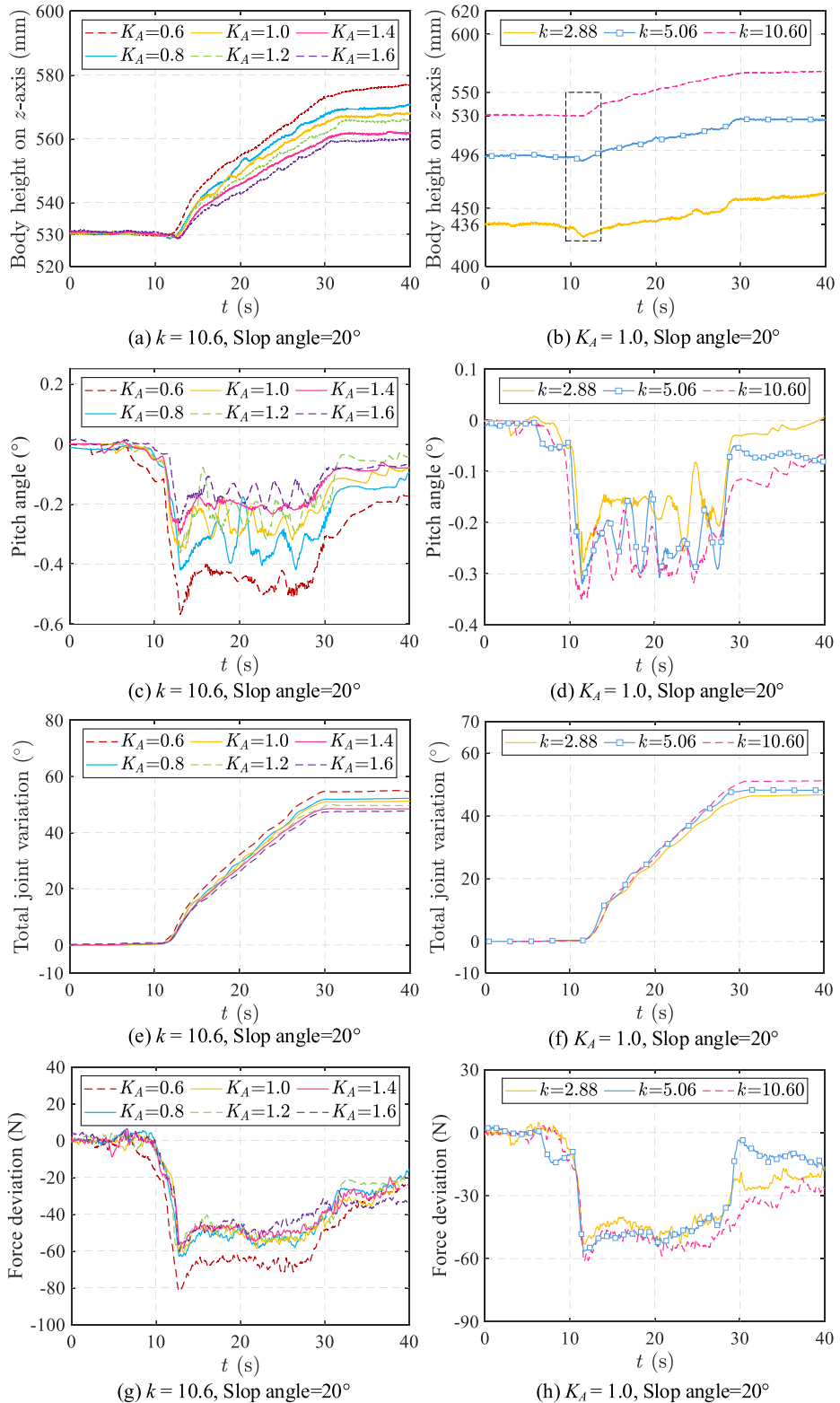


Fig. 17. Experiment comparisons based on Terrain A.

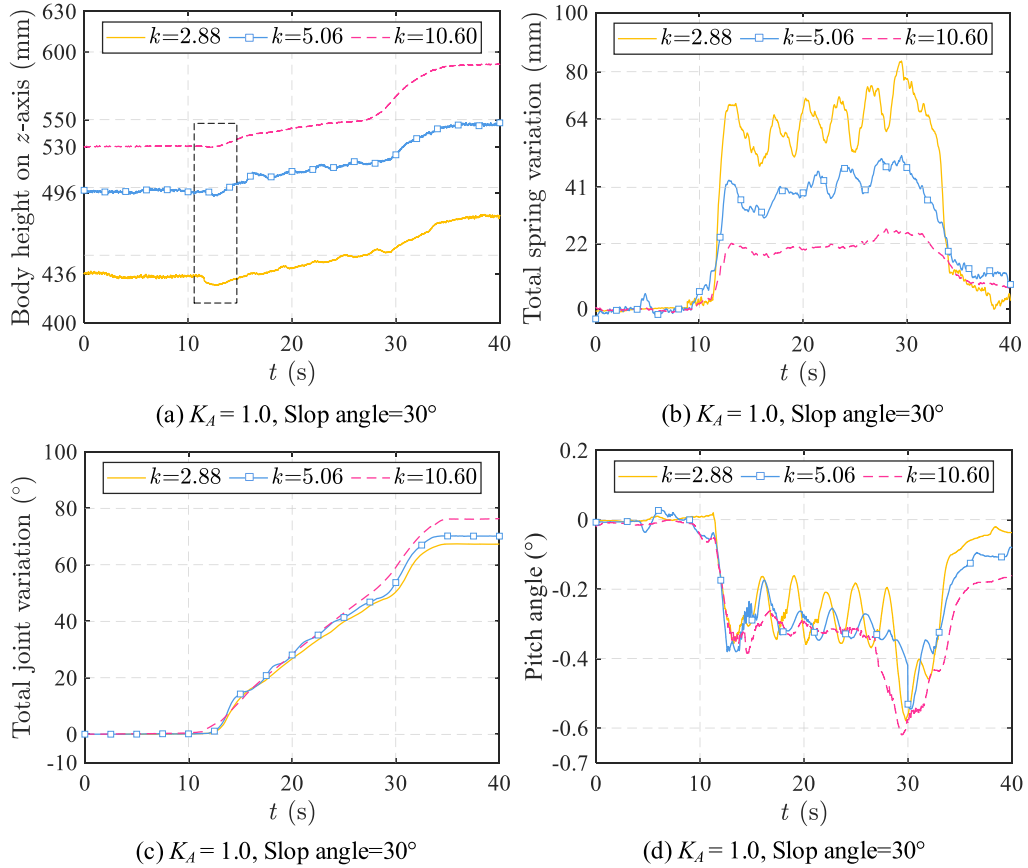


Fig. 18. Experiment comparisons based on Terrain B.

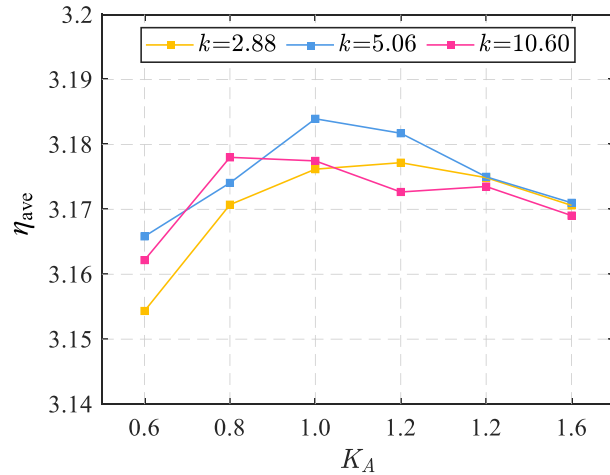


Fig. 19. Comprehensive performance evaluation under different stiffness combinations.

multiple generations. By repeatedly applying selection, crossover, and mutation operators, it converges towards the Pareto front, which represents the set of non-dominated solutions. The results of this process are depicted in Fig. 20(b). It can be seen that the results are a set of Pareto optimal solutions, which still require further analysis and interpretation to determine the best choice. Compared to the performance atlas method, it lacks graphical intuitiveness.

Table 1 compares and discusses the optimization methods used for solving multi-objective problems. The weighted sum method

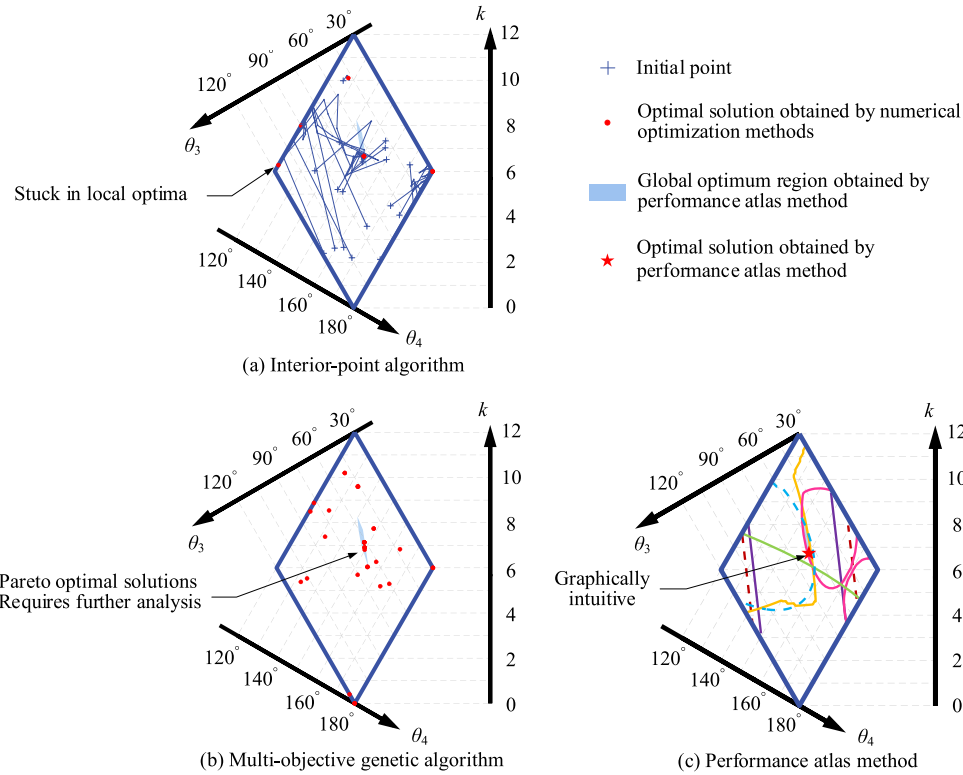


Fig. 20. Comparisons of different optimization methods, i.e. interior-point algorithm, multi-objective genetic algorithm, performance atlas method: solution, solving process, and visualization.

transforms the multi-objective optimization problem into a single-objective optimization problem. It may get stuck in local optima. And it is challenging to discern the relationship between different objectives. However, it has the lowest complexity. By utilizing the interior-point algorithm, the theoretical complexity of linear programming (LP) ranges from $O(n^{1.5}L) \sim O(n^3L)$, and nonlinear programming (NLP) typically has an overall complexity of $O(n^{4.5}L)$, where, n represents the number of variables, L is the bit length of the input data.

The Pareto optimization method obtains the Pareto optimal set and then further selects the best solution from this set. When there are more than three optimization objectives, the Pareto front becomes high-dimensional and difficult to visualize. The complexity of the multi-objective genetic algorithm primarily depends on the population size, number of generations, and the number of objectives.

The performance atlas method allows for an intuitive selection of the optimal solution from a graphical representation. It maintains the independence of each optimization objective and avoids getting stuck in local optima. The trade-offs between different optimization objectives can be intuitively observed from the graph. However, the performance atlas method exhaustively explores every possible solution, resulting in the highest complexity.

6. Conclusions and discussions

This paper conducts the stiffness optimization design for a wheeled-legged rover with both active and passive compliance capabilities. The stiffness of the suspension system affects its ability to adapt to uneven terrains, load capacity, body stability, and energy consumption. Therefore, optimizing the active and passive stiffness combination is crucial for enhancing the comprehensive performance of the system. The kinematic model of the system is first established. For a series-parallel hybrid system with 20 DoFs and passive springs, a precise kinematic model is fundamental for describing the motion characteristics of the system. Secondly, individual performance indices are derived, including the deformation coefficient, load capacity coefficient, dynamic stability coefficient, and ACE distribution coefficient. Thirdly, a multi-objective optimization method is utilized to find the optimum stiffness parameters. The optimization parameters, constraints, and systematic performance evaluation criteria are analyzed. Finally, each performance index is subjected to individual numerical calculation and analysis. The global optimum region and optimum stiffness combination are then determined. Experiments have been conducted on the TAWL rover, utilizing two different uneven terrains with varying slope angles and heights to validate the applicability of the designed stiffness. Different stiffness combinations are tested. Due to the inability to purchase springs that exactly match the optimized stiffness results, experiments indicate that the stiffness combination closest to the optimized results yields the best comprehensive performance.

Table 1
Comparisons and discussions among different multi-objective optimization methods.

| | Success rate | | Visualization | | Complexity | |
|----------------------------|--------------|--|---------------|--|------------|--|
| | Score | Reason | Score | Reason | Score | Reason |
| Weighted sum method | ●○○ | May get stuck in local optima | ●○○ | By repeating the optimization multiple times and plotting the results on the graph, the global optimal solution can be selected from the local optima. | ●●● | Using interior-point algorithm to solve LP and NLP problems: $O(n^{1.5} L) \sim O(n^4 L)$ where n is the number of variables, L is the bit length of the input data. Lowest complexity. |
| Pareto optimization method | ●●○○ | Obtain the Pareto optimal set, then further select the best solution from the set. | ●○○ | When there are more than three optimization objectives, the Pareto front is high-dimensional and difficult to visualize. | ●●○○ | Using multi-objective genetic algorithm to solve the problem: $O(G \times M \times N^2)$ where G is the number of generations, M is the number of objectives, N is the population size. Medium complexity |
| Performance atlas method | ●●● | Intuitively select the optimal solution from the graph. | ●●● | The trade-offs between optimization objectives can be intuitively observed from the graph. | ●○○ | $O(m^n)$ where m is the number of possible values for each variable, n is the number of variables. Highest complexity. |

This paper advances the stiffness design of active and passive compliant systems by establishing a compliance model and optimizing stiffness parameters, thereby enhancing the terrain adaptability of the system. Future work will involve more complex control methods, incorporating variable optimum stiffness parameters and robust physical prototype experiments for real-world planetary applications purposes.

CRediT authorship contribution statement

Bike Zhu: Writing – original draft, Visualization, Validation. **Jun He:** Writing – review & editing, Supervision, Funding acquisition. **Feng Gao:** Writing – review & editing, Supervision.

Declaration of competing interest

The authors declare that they have no known competing financial interests or personal relationships that could have appeared to influence the work reported in this paper.

Data availability

No data was used for the research described in the article.

Acknowledgments

This research was funded by the National Natural Science Foundation of China under Grant 52175022.

References

- [1] T. Paty, N. Binaud, S. Caro, et al., Cable-driven parallel robot modelling considering pulley kinematics and cable elasticity, *Mech. Mach. Theory* 159 (2021) 104263.
- [2] J. He, J. Li, Z. Sun, et al., Kinematic design of a serial-parallel hybrid finger mechanism actuated by twisted-and-coiled polymer, *Mech. Mach. Theory* 152 (2020) 103951.
- [3] W. Zeng, G. Xu, H. Jiang, et al., Design of a variable-diameter wheel with a novel distributed compliant mechanism, *Mech. Mach. Theory* 189 (2023) 105450.
- [4] J. Chen, Z. Liang, Y. Zhu, et al., Towards the exploitation of physical compliance in segmented and electrically actuated robotic legs: a review focused on elastic mechanisms, *Sensors* 19 (2019) 5351.
- [5] M. Hutter, C. Gehring, M.A. Höpflinger, et al., Toward combining speed, efficiency, versatility, and robustness in an autonomous quadruped, *IEEE Trans. Robot.* 30 (2014) 1427–1440.
- [6] M. Hutter, C.D. Remy, M.A. Hoepflinger, et al., Efficient and versatile locomotion with highly compliant legs, *IEEE Trans. Mechatron.* 18 (2013) 449–458.
- [7] B. Na, K. Kong, Design of a one degree-of-freedom quadruped robot based on a mechanical link system: cheetahoid-II, *IFAC PapersOnLine* 49 (2016) 409–415.
- [8] E. Koco, A. Mutka, Z. Kovacic, New variable passive-compliant element design for quadruped adaptation to stiffness-varying terrain, *Int. J. Adv. Robot. Syst.* 13 (2016) 90.
- [9] Y. Han, W. Guo, Z. Peng, et al., Dimensional Synthesis of the reconfigurable legged mobile lander with multi-mode and complex mechanism topology, *Mech. Mach. Theory* 155 (2021) 104097.
- [10] S. Lin, Y. Song, H. Wang, et al., Variable curvature adaptation and transformation flow of a passive-compliant magnetic wheeled wall-climbing robot, *Mech. Mach. Theory* 189 (2023) 105440.
- [11] A. Sprowitz, A. Tuleu, M. Vespignani, et al., Towards dynamic trot gait locomotion: design, control, and experiments with Cheetah-cub, a compliant quadruped robot, *Int. J. Robot. Res.* 32 (2013) 932–950.
- [12] W. Roozing, Z. Ren, N.G. Tsagarakis, An efficient leg with series-parallel and biarticular compliant actuation: design optimization, modeling, and control of the eLeg, *Int. J. Robot. Res.* 40 (1) (2021) 37–54.
- [13] L. Ni, L. Wu, H. Zhang, Parameters uncertainty analysis of posture control of a four-wheel-legged robot with series slow active suspension system, *Mech. Mach. Theory* 175 (2022) 104966.
- [14] K. Xu, Y. Lu, L. Shi, et al., Whole-body stability control with high contact redundancy for wheel-legged hexapod robot driving over rough terrain, *Mech. Mach. Theory* 181 (2023) 105199.
- [15] M. Okada, Y. Nakamura, S. Hoshino, Design of active/passive hybrid compliance in the frequency domain-shaping dynamic compliance of humanoid shoulder mechanism, in: Proceedings of the IEEE ICRA, San Francisco, CA, USA 3, 2000, pp. 2250–2257.
- [16] J. Gurney, A.S. Filsoofi, E. McClain, et al., UPed: a quadruped robot platform to study directional leg compliance, *J. Mech. Robot.* 15 (2023).
- [17] A. Nasr, S. Bell, J. McPhee, Optimal design of active-passive shoulder exoskeletons: a computational modeling of human-robot interaction, *Multibody Syst. Dyn.* 57 (1) (2023) 73–106.
- [18] A. Brahmia, R. Kelaiaia, O. Company, et al., Kinematic sensitivity analysis of manipulators using a novel dimensionless index, *Robot. Auton. Syst.* 150 (2022) 104021.
- [19] R.J. Wang, H.P. Huang, An active-passive variable stiffness elastic actuator for safety robot systems, in: Proceedings of the IEEE/RSJ International Conference on Intelligent Robots and Systems, Taipei, Taiwan, 2010, pp. 3664–3669.
- [20] L. Bai, J. Guan, X. Chen, et al., An optional passive/active transformable wheel-legged mobility concept for search and rescue robots, *Robot. Auton. Syst.* 107 (2018) 145–155.
- [21] M. Dorigo, M. Birattari, T. Stutzle, Ant colony optimization, *IEEE Comput. Intell. Mag.* 1 (4) (2006) 28–39.
- [22] J. Kennedy, R.C. Eberhart, A discrete binary version of the particle swarm algorithm, in: Proceedings of the IEEE International Conference on Systems, Man, and Cybernetics, Orlando, FL, USA 5, 1997, pp. 4104–4108.
- [23] M. Mitchell, An Introduction to Genetic Algorithms, MIT Press, 1998.
- [24] A. Brahmia, A. Kerboua, R. Kelaiaia, et al., Tolerance synthesis of delta-like parallel robots using a nonlinear optimisation method, *Appl. Sci.* 13 (19) (2023) 10703.
- [25] Y. Han, W. Guo, F. Gao, et al., A new dimension design method for the cantilever-type legged lander based on truss-mechanism transformation, *Mech. Mach. Theory* 142 (2019) 103611.

- [26] F. Gao, X.Q. Zhang, Y.S. Zhao, et al., Distribution of some properties in physical model of the solution space of 2-DOF parallel planar manipulators, *Mech. Mach. Theory* 30 (6) (1995) 811–817.
- [27] R. Kelaiaia, A. Chemori, A. Brahmia, et al., Optimal dimensional design of parallel manipulators with an illustrative case study: a review, *Mech. Mach. Theory* 188 (2023) 105390.
- [28] J. Tang, S. Yao, R. Liu, et al., A Schatz-based omnidirectional mobile mechanism with Oloid-like paddlewheels, *Mech. Mach. Theory* 189 (2023) 105434.
- [29] M. Russo, S. Herrero, O. Altuzarra, et al., Kinematic analysis and multi-objective optimization of a 3-UPR parallel mechanism for a robotic leg, *Mech. Mach. Theory* 120 (2018) 192–202.
- [30] X.J. Liu, J. Wang, G. Pritschow, Performance atlases and optimum design of planar 5R symmetrical parallel mechanisms, *Mech. Mach. Theory* 41 (2) (2006) 119–144.
- [31] Y. Han, W. Guo, D. Zhao, et al., Multi-mode unified modeling and operation capability synergistic evaluation for the reconfigurable legged mobile lander, *Mech. Mach. Theory* 171 (2022) 104714.
- [32] B. Zhu, J. He, J. Sun, Kinematic modeling and hybrid motion planning for wheeled-legged rovers to traverse challenging terrains, *Robotica* 42 (1) (2024) 153–178.
- [33] J. He, Y. Sun, L. Yang, et al., Design and control of TAWL-a wheel-legged rover with terrain-adaptive wheel speed allocation capability, *IEEE/ASME Trans. Mechatron.* 27 (4) (2022) 2212–2223.
- [34] T. Gold, A. Völz, K. Graichen, External torque estimation for an industrial robot arm using joint torsion and motor current measurements, *IFAC-PapersOnLine* 52 (15) (2019) 352–357.